Geosci. Model Dev. Discuss., 3, 1939–2019, 2010
www.geosci-model-dev-discuss.net/3/1939/2010/
doi:10.5194/gmdd-3-1939-2010

Geoscientific Model Development Discussions

MEDUSA: a new intermediate complexity plankton ecosystem model for the global domain

A. Yool, E. E. Popova, and T. R. Anderson

National Oceanography Centre; University of Southampton Waterfront Campus, European Way, Southampton SO14 3ZH, UK

Received: 25 June 2010 – Accepted: 30 September 2010 – Published: 29 October 2010

Correspondence to: A. Yool (axy@noc.soton.ac.uk)

Published by Copernicus Publications on behalf of the European Geosciences Union.

Abstract

The ongoing, anthropogenically-driven changes to the global ocean are expected to have significant consequences for plankton ecosystems in the future. Because of the role that plankton play in the ocean's "biological pump", changes in abundance, distribution and productivity will likely have additional consequences for the wider carbon cycle. Just as in the terrestrial biosphere, marine ecosystems exhibit marked diversity in species and functional types of organisms. Predicting potential change in plankton ecosystems therefore requires the use of models that are suited to this diversity, but whose parameterisation also permits robust and realistic functional behaviour. In the past decade, advances in model sophistication have attempted to address diversity, but have been criticised for doing so inaccurately or ahead of a requisite understanding of underlying processes. Here we introduce *MEDUSA* (**M**odel of **E**cosystem **D**ynamics, nutrient **U**tilisation, **S**equestration and **A**cidification), a new "intermediate complexity" plankton ecosystem model that expands on traditional nutrient-phytoplankton-zooplankton-detritus (NPZD) models, and remains amenable to global-scale evaluation. *MEDUSA* includes the biogeochemical cycles of nitrogen, silicon and iron, broadly structured into "small" and "large" plankton size classes, of which the "large" phytoplankton class is representative of a key phytoplankton group, the diatoms. A full description of *MEDUSA*'s state variables, differential equations, functional forms and parameter values is included, with particular attention focused on the submodel describing the export of organic carbon from the surface to the deep ocean. *MEDUSA* is used here in a multi-decadal hindcast simulation, and its biogeochemical performance evaluated at the global scale.

1 Introduction

Marine biota play a key role in the cycling and sequestering carbon in the ocean via the so-called "biological pump" (Raven and Falkowski, 1999). Fuelled by nutrients upwelled from the deep, phytoplankton produce organic matter via photosynthesis in the sunlit

surface ocean. This is then processed by components of the marine ecosystem including grazing zooplankton, and a fraction exported back to depth via sinking detrital particles and dissolved organic matter. This biogenic flux of carbon into the deep ocean serves to elevate the ocean's storage of carbon beyond that sequestered through physics and chemistry alone. While the large-scale role of biology can be studied from its effects on tracer distributions (e.g. Gruber et al., 1996), mathematical modelling provides an important means of investigating the dynamics of the biological pump and its response to changing climate.

For many years, nutrient-phytoplankton-zooplankton-detritus (NPZD) models were the mainstay of basin- and global-scale biogeochemical modelling studies (e.g. Sarmiento et al., 1993; Six and Maier-Reimer, 1996; Palmer and Totterdell, 2001). Today, aggregating the wide taxonomic and functional diversity of organisms in marine ecosystems into such an idealised model structure is generally considered too simplistic an approach. In the case of phytoplankton, for example, there are numerous different groups, so called plankton functional types (PFTs) such as diatoms, nitrogen fixers and coccolithophores, which undertake specific roles in marine biogeochemical cycles (Hood et al., 2006). A new generation of complex models that include multiple PFTs has accordingly been developed (e.g. Moore et al., 2004; Gregg et al., 2003; Le Quéré et al., 2005), yet complexity in models has associated difficulties including poorly understood ecology, lack of data for validation and sensitivity to the parameterisations involved (Anderson, 2005; Flynn, 2005). Additionally, on a practical level, the greater the complexity of an ecosystem model, the greater the computation burden involved in its simulation, and therefore the less attractive the model is for long duration simulations of, for instance, future climate change (e.g. Cox et al., 2000).

The challenge is to derive model structures and parameterisations that are robust in the sense that the modelled ecosystem reacts realistically with the physico-chemical environment, yet which are based on sound mechanistic principles that maintain accuracy in prediction (Anderson, 2010). Here, we present a new ecosystem model, *MEDUSA*, and show results for its performance when incorporated

into a global ocean general circulation model (GCM). The *MEDUSA* model is of intermediate complexity, building beyond the standard NPZD formulations, but without elaborating to the number of state variables and parameters in contemporary PFT models. The plankton ecosystem is divided into "small" and "large" portions, into which different planktonic components are organised. The small portion primarily includes (prokaryotic) nanophytoplankton and microzooplankton (protists and larval metazoans), together with small detrital particles that sink relatively slowly and are explicitly represented. The large portion primarily includes (eukaryotic) diatom phytoplankton and mesozooplankton (adult metazoans), together with large detrital particles that are assumed to sink sufficiently quickly that implicit representation is required. The phytoplankton components of *MEDUSA* include explicit representations of internal chlorophyll quotas, in order that light acclimation is permitted. The resulting plankton ecosystem is founded on the biogeochemical cycle of nitrogen, although the cycles of silicon and the micronutrient iron are also included.

The layout of the manuscript is as follows. First, *MEDUSA*'s structure, differential equations, functional forms and parameterisation are fully described. Since *MEDUSA* has a particular focus on the biologically-driven sequestration of carbon in the deep ocean, the particulate flux submodels are described in detail. Next, *MEDUSA* is used in a standard control simulation for the period 1958 to 2005 (inclusive), and its performance assessed for the global ocean. This simulation makes use of a medium resolution instance of the Nucleus for European Modelling of the Ocean (NEMO) physical model (Madec, 2008) into which *MEDUSA* is embedded. Finally, the results of this simulation are discussed within the context of the need to move beyond NPZD models and to include additional factors associated with the biological carbon pump, such as ecosystem structure and multiple nutrient interaction.

2 *MEDUSA*

2.1 State variables

The model resolves 11 state variables distributed between the nitrogen (6), silicon (2) and iron (1) cycles. The remaining 2 state variables denote chlorophyll for each of the 2 phytoplankton classes. Nitrogen is the model's primary currency. The biogeochemical cycling of major elements in marine systems often exhibits relatively constant stoichiometry in which the ratios of utilisation of inorganic carbon, nitrogen and phosphorus by phytoplankton are matched by corresponding ratios of remineralisation in the deep ocean (Redfield, 1934). This has been particularly convenient for modellers because the cycling of nutrients by the marine ecosystem can be converted to carbon by simply multiplying by the so-called "Redfield ratio". Examples of this approach being used in GCMs include Six and Maier-Reimer (1996), Palmer and Totterdell (2001), Moore et al. (2004) and Le Quéré et al. (2005). We adopt the same approach here whereby the fluxes of carbon are calculated empirically from those of nitrogen without the need for explicit carbon tracers. Additional tracers for dissolved inorganic carbon (DIC) and alkalinity can be added for simulations that require a complete oceanic carbon cycle (e.g. for air-sea CO_2 fluxes). Figure 1 presents a diagrammatic representation of *MEDUSA*'s components and the relationships between them. The state variables are:

Pn	Non-diatom phytoplankton	mmol N m^{-3}
Pd	Diatom phytoplankton	mmol N m^{-3}
Chl_{Pn}	Chlorophyll in non-diatoms	mg chl m^{-3}
Chl_{Pd}	Chlorophyll in diatoms	mg chl m^{-3}
Pd_{Si}	Diatom phytoplankton (silicon)	mmol Si m^{-3}
Zμ	Microzooplankton	mmol N m^{-3}
Zm	Mesozooplankton	mmol N m^{-3}

D	Slow-sinking detritus	mmol N m^{-3}
N	Nitrogen nutrient	mmol N m^{-3}
S	Silicic acid	mmol Si m^{-3}
F	Iron nutrient	mmol Fe m^{-3}

The model includes a number of notable features. First, *MEDUSA* includes a stoichiometric representation of the trophic transfer of carbon and nitrogen during feeding by zooplankton, based on the C:N ratios in predator and prey, and derived from the model of Anderson and Hessen (1995) (based on the implementation in Anderson and Pondaven, 2003). Second, *MEDUSA* adds an explicit diatom silicon state variable (Pd_{Si}) to allow diatom cells to have a dynamic Si:N ratio, based on the model of Mongin et al. (2006). Third, *MEDUSA* includes both slow- and fast-sinking detrital pathways to represent the transport of particulate organic carbon in the ocean interior. The former is represented explicitly with a defined sinking rate, while the latter implicitly represents large particles that sink too quickly to be properly resolved within model time-stepping. The modifications adopted here for fast-sinking detritus are based on the ballast model of Armstrong et al. (2002), with the specific implementation derived largely from Dunne et al. (2007). Finally, *MEDUSA* adds an iron cycle submodel and explicit iron state variable (F) to permit regional phytoplankton limitation by this important micronutrient. As remarked upon by Galbraith et al. (2010), iron submodels are still rudimentary, and there is significant uncertainty concerning the detail of the ocean's iron cycle. Consequently, here we adopt the relatively simple iron submodel of Parekh et al. (2005) (based on the implementation in Dutkiewicz et al., 2005). In this, model iron is linked in a single fixed ratio to nitrogen throughout the ecosystem, but it also experiences processes that add (aeolian deposition) and remove (scavenging) it from the water column.

A key intention in this choice of framework is that *MEDUSA* separately represents populations of small phytoplankton that are strongly controlled by fast-growing microzooplankton, and those of large phytoplankton that are more weakly controlled

by slower-growing mesozooplankton. Since diatoms form a key component of larger phytoplankton (Mann, 1999), *MEDUSA* assumes that they are synonymous with modelled "large phytoplankton". This assumption simplifies the real world situation in which even diatom species span a range of cell sizes (Furnas, 1990). Further assumptions concerning *MEDUSA*'s phytoplankton include faster growth and better nutrient uptake kinetics of the small phytoplankton (Furnas, 1990), and similar size-linked growth patterns in zooplankton (Baird and Suthers, 2007).

2.2 Differential equations

The following equations describe the tendency terms operating on the biogeochemical state variables in the model. Abbreviations used are: "PP" for primary production; "µzoo" for microzooplankton; "mzoo" for mesozooplankton; "non-lin" for non-linear; "remin" for remineralisation. Functions and parameters are defined in Sects. 2.3 and 2.4.

$$\frac{\partial \mathrm{Pn}}{\partial t} = +\underbrace{[\mathrm{PP}_{\mathrm{Pn}} \cdot \mathrm{Pn}]}_{\text{non-diatom PP}} - \underbrace{[\mathrm{G}\mu_{\mathrm{Pn}}]}_{\mu\text{zoo graze}} - \underbrace{[\mathrm{Gm}_{\mathrm{Pn}}]}_{\text{mzoo graze}} - \underbrace{[\mathrm{M1}_{\mathrm{Pn}}]}_{\text{linear losses}} - \underbrace{[\mathrm{M2}_{\mathrm{Pn}}]}_{\text{non-lin losses}} \quad (1)$$

$$\frac{\partial \mathrm{Pd}}{\partial t} = +\underbrace{[\mathrm{PP}_{\mathrm{Pd}} \cdot \mathrm{Pd}]}_{\text{diatom PP}} - \underbrace{[\mathrm{Gm}_{\mathrm{Pd}}]}_{\text{mzoo graze}} - \underbrace{[\mathrm{M1}_{\mathrm{Pd}}]}_{\text{linear losses}} - \underbrace{[\mathrm{M2}_{\mathrm{Pd}}]}_{\text{non-lin losses}} \quad (2)$$

$$\frac{\partial \mathrm{Chl}_{\mathrm{Pn}}}{\partial t} = \left(+\underbrace{[R_{\mathrm{Pn}} \cdot \mathrm{PP}_{\mathrm{Pn}} \cdot \mathrm{Pn}]}_{\text{non-diatom PP}} - \underbrace{[\mathrm{G}\mu_{\mathrm{Pn}}]}_{\mu\text{zoo graze}} - \underbrace{[\mathrm{Gm}_{\mathrm{Pn}}]}_{\text{mzoo graze}} - \underbrace{[\mathrm{M1}_{\mathrm{Pn}}]}_{\text{linear losses}} - \underbrace{[\mathrm{M2}_{\mathrm{Pn}}]}_{\text{non-lin losses}} \right) \cdot \theta_{\mathrm{Pn}}^{\mathrm{Chl}} \cdot \xi^{-1} \quad (3)$$

$$\frac{\partial \mathrm{Chl}_{\mathrm{Pd}}}{\partial t} = \left(+\underbrace{[R_{\mathrm{Pd}} \cdot \mathrm{PP}_{\mathrm{Pd}} \cdot \mathrm{Pd}]}_{\text{diatom PP}} - \underbrace{[\mathrm{Gm}_{\mathrm{Pd}}]}_{\text{mzoo graze}} - \underbrace{[\mathrm{M1}_{\mathrm{Pd}}]}_{\text{linear losses}} - \underbrace{[\mathrm{M2}_{\mathrm{Pd}}]}_{\text{non-lin losses}} \right) \cdot \theta_{\mathrm{Pd}}^{\mathrm{Chl}} \cdot \xi^{-1} \quad (4)$$

$$\frac{\partial \mathrm{Pd}_{\mathrm{Si}}}{\partial t} = +\underbrace{\left[\mathrm{PP}_{\mathrm{Pd}_{\mathrm{Si}}} \cdot \mathrm{Pd}_{\mathrm{Si}}\right]}_{\text{diatom PP}} - \underbrace{\left[\mathrm{Gm}_{\mathrm{Pd}_{\mathrm{Si}}}\right]}_{\text{mzoo graze}} - \underbrace{\left[\mathrm{M1}_{\mathrm{Pd}_{\mathrm{Si}}}\right]}_{\text{linear losses}} - \underbrace{\left[\mathrm{M2}_{\mathrm{Pd}_{\mathrm{Si}}}\right]}_{\text{non-lin losses}} - \underbrace{\left[\mathrm{DS}_{\mathrm{Pd}_{\mathrm{Si}}}\right]}_{\text{dissolution}} \quad (5)$$

$$\frac{\partial \mathrm{Z}\mu}{\partial t} = +\underbrace{\left[F_{\mathrm{Z}\mu}\right]}_{\text{all grazing}} - \underbrace{\left[\mathrm{Gm}_{\mathrm{Z}\mu}\right]}_{\text{mzoo graze}} - \underbrace{\left[\mathrm{M1}_{\mathrm{Z}\mu}\right]}_{\text{linear losses}} - \underbrace{\left[\mathrm{M2}_{\mathrm{Z}\mu}\right]}_{\text{non-lin losses}} \quad (6)$$

$$\frac{\partial \mathrm{Zm}}{\partial t} = +\underbrace{[F_{\mathrm{Zm}}]}_{\text{all grazing}} - \underbrace{[\mathrm{M1}_{\mathrm{Zm}}]}_{\text{linear losses}} - \underbrace{[\mathrm{M2}_{\mathrm{Zm}}]}_{\text{non-lin losses}} \quad (7)$$

$$\begin{aligned}\frac{\partial \mathrm{D}}{\partial t} = {} & + \underbrace{[\mathrm{M2}_{\mathrm{Pn}}]}_{\text{non-diatom losses}} + \underbrace{\left[(1-\mathrm{D1}_{\mathrm{frac}}) \cdot \mathrm{M2}_{\mathrm{Pd}}\right]}_{\text{diatom losses}} + \underbrace{\left[\mathrm{M2}_{\mathrm{Z}\mu}\right]}_{\mu\text{zoo losses}} + \underbrace{\left[(1-\mathrm{D2}_{\mathrm{frac}}) \cdot \mathrm{M}_{\mathrm{Zm}}\right]}_{\text{mzoo losses}} \\ & + \underbrace{\left[(1-\beta_{\mathrm{N}}) \cdot \mathrm{IN}_{\mathrm{Z}\mu}\right]}_{\mu\text{zoo egestion}} + \underbrace{[(1-\beta_{\mathrm{N}}) \cdot \mathrm{IN}_{\mathrm{Zm}}]}_{\text{mzoo egestion}} - \underbrace{[\mathrm{G}\mu_{\mathrm{D}}]}_{\mu\text{zoo graze}} - \underbrace{[\mathrm{Gm}_{\mathrm{D}}]}_{\text{mzoo graze}} - \underbrace{[\mathrm{M}_{\mathrm{D}}]}_{\text{remin}} - \underbrace{\left[w_{\mathrm{g}} \cdot \frac{\partial \mathrm{D}}{\partial z}\right]}_{\text{sinking}}\end{aligned} \quad (8)$$

$$\begin{aligned}\frac{\partial \mathrm{N}}{\partial t} = {} & -\underbrace{[\mathrm{PP}_{\mathrm{Pn}} \cdot \mathrm{Pn}]}_{\text{non-diatom PP}} - \underbrace{[\mathrm{PP}_{\mathrm{Pd}} \cdot \mathrm{Pd}]}_{\text{diatom PP}} + \underbrace{[\phi \cdot (\mathrm{G}\mu_{\mathrm{Pn}} + \mathrm{G}\mu_{\mathrm{D}})]}_{\mu\text{zoo messy feeding}} \\ & + \underbrace{\left[\phi \cdot (\mathrm{Gm}_{\mathrm{Pn}} + \mathrm{Gm}_{\mathrm{Pd}} + \mathrm{Gm}_{\mathrm{Z}\mu} + \mathrm{Gm}_{\mathrm{D}})\right]}_{\text{mzoo messy feeding}} \\ & + \underbrace{[\mathrm{M1}_{\mathrm{Pn}}]}_{\text{non-diatom losses}} + \underbrace{[\mathrm{M1}_{\mathrm{Pd}}]}_{\text{diatom losses}} + \underbrace{\left[\mathrm{M1}_{\mathrm{Z}\mu}\right]}_{\mu\text{zoo losses}} + \underbrace{[\mathrm{M1}_{\mathrm{Zm}}]}_{\text{mzoo losses}} + \underbrace{[\mathrm{M}_{\mathrm{D}}]}_{\text{remin}} + \underbrace{[\mathrm{LD}_{\mathrm{N}}(z) \cdot T_{\mathrm{N}}]}_{\text{fast N detritus remin}}\end{aligned} \quad (9)$$

$$\frac{\partial \mathrm{S}}{\partial t} = -\underbrace{\left[\mathrm{PP}_{\mathrm{Pd}_{\mathrm{Si}}} \cdot \mathrm{Pd}_{\mathrm{Si}}\right]}_{\text{diatom PP}} + \underbrace{\left[\mathrm{M1}_{\mathrm{Pd}_{\mathrm{Si}}}\right]}_{\text{linear losses}} + \underbrace{\left[(1-\mathrm{D1}_{\mathrm{frac}}) \cdot \mathrm{M2}_{\mathrm{Pd}_{\mathrm{Si}}}\right]}_{\text{non-lin. losses}} + \underbrace{\left[\mathrm{DS}_{\mathrm{Pd}_{\mathrm{Si}}}\right]}_{\text{dissolution}}$$

$$+\underbrace{\left[(1-\mathrm{D2_{frac}})\cdot \mathrm{Gm_{Pd_{Si}}}\right]}_{\text{mzoo graze}}+\underbrace{\left[\mathrm{LD_{Si}}(z)\cdot T_{\mathrm{Si}}\right]}_{\text{fast Si detritus remin}} \tag{10}$$

$$\frac{\partial \mathrm{F}}{\partial t}=-\underbrace{\left[R_{\mathrm{Fe}}\cdot\frac{\partial \mathrm{N}}{\partial t}\right]}_{\text{coupled to N}}+\underbrace{\left[\mathrm{F_{atmos}}\right]}_{\text{aeolian}}-\underbrace{\left[\mathrm{F_{scavenge}}\right]}_{\text{scavenging}} \tag{11}$$

These differential equations are applied to the biogeochemical state variables within every ocean grid cell in the physical model, regardless of horizontal or vertical position. This parallels the implementation of ecosystem models in some general circulation models (e.g. Yool et al., 2010), but is different from other studies in which different equations are applied at different depths, typically to separate the photic and aphotic zones (e.g. Popova et al., 2006).

2.3 Interaction functional forms

The following series of equations expand on the tendency terms described in the differential equations. Parameter definitions and values are described in Sect. 2.4.

2.3.1 Non–diatom limitation and growth

The chlorophyll and light-limited growth terms for non-diatom phytoplankton are derived from those in Taylor et al. (1997) and Fasham et al. (1990), and based on their implementation in Popova et al., 2006. As per Eppley (1972), maximum phytoplankton growth rate is a simple exponential function of temperature. Nutrient limitation is factored in through standard Michaelis-Menten terms.

$$\theta_{\mathrm{Pn}}^{\mathrm{Chl}}=\frac{\mathrm{Chl_{Pn}}\cdot\xi}{\mathrm{Pn}} \tag{12}$$

$$\hat{\alpha}_{\mathrm{Pn}}=\alpha_{\mathrm{Pn}}\cdot\theta_{\mathrm{Pn}}^{\mathrm{Chl}} \tag{13}$$

$\theta_{\mathrm{Pn}}^{\mathrm{Chl}}$ is the scaled chlorophyll to biomass ratio, while $\hat{\alpha}_{\mathrm{Pn}}$ scales the initial slope of the photosynthesis-irradiance (P-I) curve, α_{Pn}, by this ratio so that phytoplankton with a high chlorophyll content have an elevated response to irradiance.

$$V_{\mathrm{Pn}^T}=V_{\mathrm{Pn}}\cdot 1.066^T \tag{14}$$

This term calculates maximum phytoplankton growth rate as an exponential function of temperature and base growth rate at 0°C.

$$J_{\mathrm{Pn}}=\frac{V_{\mathrm{Pn}^T}\cdot\hat{\alpha}_{\mathrm{Pn}}^2\cdot I^2}{(V_{\mathrm{Pn}^T}^2+\hat{\alpha}_{\mathrm{Pn}}^2\cdot I^2)^{1/2}} \tag{15}$$

Given the (chlorophyll-related) initial slope of the P-I curve and (temperature-related) maximum phytoplankton growth rate, this function calculates realised growth rate given local irradiance, I.

$$Q_{\mathrm{N,\,Pn}}=\frac{\mathrm{N}}{k_{\mathrm{N,\,Pn}}+\mathrm{N}} \tag{16}$$

$$Q_{\mathrm{Fe,\,Pn}}=\frac{\mathrm{F}}{k_{\mathrm{Fe,\,Pn}}+\mathrm{F}} \tag{17}$$

Nutrient limitation of phytoplankton growth is specified here via standard, hyperbolic Michaelis-Menten terms that use ambient nutrient concentrations and parameters for the concentration at which phytoplankton growth is half its theoretical maximum.

$$\mathrm{PP_{Pn}}=J_{\mathrm{Pn}}\cdot Q_{\mathrm{N,\,Pn}}\cdot Q_{\mathrm{Fe,\,Pn}} \tag{18}$$

Light- and nutrient-limitation factors are brought together in a multiplicative term that determines nutrient uptake and, via Redfield coupling, primary production.

2.3.2 Diatom limitation and growth

Diatom phytoplankton growth terms are derived from the same sources as those of non-diatom phytoplankton. However, diatom growth is additionally coupled to the silicon cycle, and the submodel of silicon uptake and diatom growth from Mongin et al. (2006) has been adopted to represent these processes. This places contraints on growth and nutrient uptake based upon the Si:N ratio of the modelled diatom cells.

$$\theta_{\mathrm{Pd}}^{\mathrm{Chl}} = \frac{\mathrm{Chl}_{\mathrm{Pd}} \cdot \xi}{\mathrm{Pd}} \tag{19}$$

$$\hat{\alpha}_{\mathrm{Pd}} = \alpha_{\mathrm{Pd}} \cdot \theta_{\mathrm{Pd}}^{\mathrm{Chl}} \tag{20}$$

$$V_{\mathrm{Pd}^T} = V_{\mathrm{Pd}} \cdot 1.066^T \tag{21}$$

$$J_{\mathrm{Pd}} = \frac{V_{\mathrm{Pd}^T} \cdot \hat{\alpha}_{\mathrm{Pd}}^2 \cdot I^2}{(V_{\mathrm{Pd}^T}^2 + \hat{\alpha}_{\mathrm{Pd}}^2 \cdot I^2)^{1/2}} \tag{22}$$

$$Q_{\mathrm{N,\,Pd}} = \frac{\mathrm{N}}{k_{\mathrm{N,\,Pd}} + \mathrm{N}} \tag{23}$$

$$Q_{\mathrm{Si}} = \frac{\mathrm{S}}{k_{\mathrm{S}} + \mathrm{S}} \tag{24}$$

$$Q_{\mathrm{Fe,\,Pd}} = \frac{\mathrm{F}}{k_{\mathrm{Fe,\,Pd}} + \mathrm{F}} \tag{25}$$

As noted above, the growth of diatom phytoplankton is additionally limited by the availability of the macronutrient silicic acid.

$$R_{\mathrm{Si:N}} = \frac{\mathrm{Pd}_{\mathrm{Si}}}{\mathrm{Pd}} \tag{26}$$

$$R_{\mathrm{N:Si}} = \frac{\mathrm{Pd}}{\mathrm{Pd}_{\mathrm{Si}}} \tag{27}$$

Silicon is largely used by diatom phytoplankton in the construction of their cell walls, or frustules, which can vary significantly in their ornamentation (e.g. spines, girdle bands; Martin-Jézéquel et al., 2000). As a result, diatoms have a degree of plasticity in their requirement for silicon, necessitating a separate state variable, and centred around the resulting stoichiometric ratios, $R_{\mathrm{Si:N}}$ and $R_{\mathrm{N:Si}}$.

$$\text{if } R_{\mathrm{Si:N}} \le R_{\mathrm{Si:N}}^0 \quad \text{then, } \mathrm{PP}_{\mathrm{Pd}} = 0 \tag{28}$$

$$\text{else if } R_{\mathrm{Si:N}}^0 < R_{\mathrm{Si:N}} < (3 \cdot R_{\mathrm{Si:N}}^0) \quad \text{then, } \mathrm{PP}_{\mathrm{Pd}} = (J_{\mathrm{Pd}} \cdot Q_{\mathrm{N,\,Pd}} \cdot Q_{\mathrm{Fe,\,Pd}}) \cdot \left(U_\infty \cdot \frac{R_{\mathrm{Si:N}} - R_{\mathrm{Si:N}}^0}{R_{\mathrm{Si:N}}} \right) \tag{29}$$

$$\text{else if } R_{\mathrm{Si:N}} \ge (3 \cdot R_{\mathrm{Si:N}}^0) \quad \text{then, } \mathrm{PP}_{\mathrm{Pd}} = (J_{\mathrm{Pd}} \cdot Q_{\mathrm{N,\,Pd}} \cdot Q_{\mathrm{Fe,\,Pd}}) \tag{30}$$

Here, the uptake of nitrogen (and iron) by diatom cells, $\mathrm{PP}_{\mathrm{Pd}}$, is governed by the Si:N ratio. If this falls below a critical value, $R_{\mathrm{Si:N}}^0$, diatom cells cannot complete their cell division cycle and growth stops Martin-Jézéquel et al. (2000). Above this minimum ratio growth is scaled by a factor of the Si:N ratio, and above 3 times this ratio, growth is unimpeded by silicon dynamics.

$$\text{if } R_{\mathrm{Si:N}} < (3 \cdot R_{\mathrm{Si:N}}^0)^{-1} \quad \text{then, } \mathrm{PP}_{\mathrm{Pd_{Si}}} = (J_{\mathrm{Pd}} \cdot Q_{\mathrm{Si}}) \tag{31}$$

$$\text{else if } (3 \cdot R_{\mathrm{Si:N}}^0)^{-1} \le R_{\mathrm{Si:N}} < (R_{\mathrm{Si:N}}^0)^{-1} \quad \text{then, } \mathrm{PP}_{\mathrm{Pd_{Si}}} = (J_{\mathrm{Pd}} \cdot Q_{\mathrm{Si}}) \cdot \left(U_\infty \cdot \frac{R_{\mathrm{N:Si}} - R_{\mathrm{N:Si}}^0}{R_{\mathrm{N:Si}}} \right) \tag{32}$$

$$\text{else if } R_{\mathrm{Si:N}} \ge (R_{\mathrm{Si:N}}^0)^{-1} \quad \text{then, } \mathrm{PP}_{\mathrm{Pd_{Si}}} = 0 \tag{33}$$

Here, silicon uptake, $PP_{Pd_{Si}}$, occurs at the maximum rate permitted by light and silicon availability whenever the Si:N ratio is below a critical threshold, $(3 \cdot R^0_{Si:N})^{-1}$. Above this ratio, silicon uptake is linearly decreased to another threshold value, $(R^0_{Si:N})^{-1}$, above which no silicon is taken up by diatom cells.

2.3.3 Chlorophyll growth scaling factors

Both phytoplankton groups have separate chlorophyll state variables in addition to those of nitrogen biomass. This allows the modelled phytoplankton to dynamically alter their chlorophyll content under different light regimes. The following terms for this processes are taken from Taylor et al. (1997).

$$R_{Pn} = \frac{\theta^{Chl}_{max}}{\theta^{Chl}_{Pn}} \cdot \frac{PP_{Pn}}{\hat{\alpha}_{Pn} \cdot I} \tag{34}$$

$$R_{Pd} = \frac{\theta^{Chl}_{max}}{\theta^{Chl}_{Pd}} \cdot \frac{PP_{Pd}}{\hat{\alpha}_{Pd} \cdot I} \tag{35}$$

2.3.4 Microzooplankton grazing

Microzooplankton graze on smaller non-diatom phytoplankton and on particles of slow-sinking detritus. The ingestion function that balances the availability of these prey items with the preference microzooplankton have for them is drawn from the classic model of Fasham et al. (1990).

$$G\mu_X = \frac{g_\mu \cdot p_{\mu X} \cdot X^2 \cdot Z\mu}{k^2_\mu + p_{\mu 1} \cdot Pn^2 + p_{\mu 2} \cdot D^2} \tag{36}$$

(37)

where X is Pn or D.

The above term is repeated for each separate prey item consumed by microzooplankton. The term is based around a sigmoid function in which the "substrate" is composed of the sum of the prey items scaled by the preference that microzooplankton have for them. It is assumed here that microzooplankton prefer non-diatom phytoplankton over detritus since they represent a higher quality food item.

$$IN_{Z\mu} = (1 - \phi) \cdot (G\mu_{Pn} + G\mu_D) \tag{38}$$

$$IC_{Z\mu} = (1 - \phi) \cdot (\theta_{Pn} \cdot G\mu_{Pn} + \theta_D \cdot G\mu_D) \tag{39}$$

Here, the separate quantities of nitrogen, $IN_{Z\mu}$, and carbon, $IC_{Z\mu}$, ingested by microzooplankton are summed, and the resulting C:N ratio calculated, $\theta_{F\mu}$.

$$\theta_{F\mu} = \frac{IC_{Z\mu}}{IN_{Z\mu}} \tag{40}$$

Since grazed material may have a different C:N ratio than that required for microzooplankton growth, the assimilation and metabolism submodel of Anderson and Pondaven (2003) is incorporated here to balance growth, excretion and respiration. The C:N ratio of ingested food calculated above is then compared to the ideal ratio preferred by microzooplankton, $\theta^*_{F\mu}$.

$$\theta^*_{F\mu} = \frac{\beta_N \cdot \theta_{Z\mu}}{\beta_C \cdot k_C} \tag{41}$$

Either C or N limits production depending on whether $\theta_{F\mu}$ is greater or lower than $\theta^*_{F\mu}$, with any excess carbon respired, and any excess nitrogen excreted. Growth, $F_{Z\mu}$, respiration, $R_{Z\mu}$, and excretion, $E_{Z\mu}$, are calculated as follows.

if $\theta_{F\mu} > \theta^*_{F\mu}$ then N is limiting and …

$$F_{Z\mu} = \beta_N \cdot IN_{Z\mu} \tag{42}$$

$$E_{Z\mu} = 0 \tag{43}$$

$$R_{Z\mu} = \left(\beta_C \cdot IC_{Z\mu}\right) - \left(\theta_{Z\mu} \cdot F_{Z\mu}\right) \tag{44}$$

else if $\theta_{F\mu} < \theta^*_{F\mu}$ then C is limiting and …

$$F_{Z\mu} = \frac{\beta_C \cdot k_C \cdot IC_{Z\mu}}{\theta_{Z\mu}} \tag{45}$$

$$E_{Z\mu} = IC_{Z\mu} \cdot \left(\frac{\beta_N}{\theta_{F\mu}} - \frac{\beta_C \cdot k_C}{\theta_{Z\mu}}\right) \tag{46}$$

$$R_{Z\mu} = \left(\beta_C \cdot IC_{Z\mu}\right) - \left(\theta_{Z\mu} \cdot F_{Z\mu}\right) \tag{47}$$

2.3.5 Mesozooplankton grazing

Mesozooplankton grazing follows that of microzooplankton with the exception that mesozooplankton have a broader range of prey items.

$$Gm_X = \frac{g_m \cdot p_{mX} \cdot X^2 \cdot Zm}{k_m^2 + F_m} \tag{48}$$

where X is Pn, Pd, Zμ or D.

$$F_m = \left(p_{m1} \cdot Pn^2\right) + \left(p_{m2} \cdot Pd^2\right) + \left(p_{m3} \cdot Z\mu^2\right) + \left(p_{m4} \cdot D^2\right) \tag{49}$$

$$Gm_{Pd_{Si}} = R_{Si} \cdot Gm_{Pd} \tag{50}$$

$$IN_{Zm} = (1 - \phi) \cdot \left(Gm_{Pd} + Gm_{Pn} + Gm_{Z\mu} + Gm_{Pd}\right) \tag{51}$$

$$IC_{Zm} = (1 - \phi) \cdot \left((\theta_{Pd} \cdot Gm_{Pd}) + (\theta_{Pn} \cdot Gm_{Pn}) + \left(\theta_{Z\mu} \cdot Gm_{Z\mu}\right) + (\theta_D \cdot Gm_D)\right) \tag{52}$$

$$\theta_{Fm} = \frac{IC_{Zm}}{IN_{Zm}} \tag{53}$$

$$\theta^*_{Fm} = \frac{\beta_N \cdot \theta_{Zm}}{\beta_C \cdot k_C} \tag{54}$$

if $\theta_{Fm} > \theta^*_{Fm}$ then N is limiting and …,

$$F_{Zm} = \beta_N \cdot IN_{Zm} \tag{55}$$

$$E_{Zm} = 0 \tag{56}$$

$$R_{Zm} = (\beta_C \cdot IC_{Zm}) - (\theta_{Zm} \cdot F_{Zm}) \tag{57}$$

else if $\theta_{Fm} < \theta^*_{Fm}$ then C is limiting and …,

$$F_{Zm} = \frac{\beta_C \cdot k_C \cdot IC_{Zm}}{\theta_{Zm}} \tag{58}$$

$$E_{Zm} = IC_{Zm} \cdot \left(\frac{\beta_N}{\theta_{Fm}} - \frac{\beta_C \cdot k_C}{\theta_{Zm}}\right) \tag{59}$$

$$R_{Zm} = (\beta_C \cdot IC_{Zm}) - (\theta_{Zm} \cdot F_{Zm}) \tag{60}$$

2.3.6 Plankton loss terms

In addition to losses to grazing, all four living components of the plankton model incur smaller, secondary losses to other processes.

$$M1_{Pn} = \mu_{1,Pn} \cdot Pn \tag{61}$$

$$M1_{Pd} = \mu_{1,Pd} \cdot Pd \tag{62}$$

$$M1_{Pd_{Si}} = R_{Si} \cdot M1_{Pd} \tag{63}$$

$$M1_{Z\mu} = \mu_{1,Z\mu} \cdot Z\mu \quad (64)$$

$$M1_{Zm} = \mu_{1,Zm} \cdot Zm \quad (65)$$

The above functions are density-independent loss terms for processes such as metabolism that occur without reference to abundance.

$$M2_{Pn} = \mu_{2,Pn} \cdot \frac{Pn}{k_{Pn} + Pn} \cdot Pn \quad (66)$$

$$M2_{Pd} = \mu_{2,Pd} \cdot \frac{Pd}{k_{Pd} + Pd} \cdot Pd \quad (67)$$

$$M2_{Pd_{Si}} = R_{Si} \cdot M2_{Pd} \quad (68)$$

$$M2_{Z\mu} = \mu_{2,Z\mu} \cdot \frac{Z\mu}{k_{Z\mu} + Z\mu} \cdot Z\mu \quad (69)$$

$$M2_{Zm} = \mu_{2,Zm} \cdot \frac{Zm}{k_{Zm} + Zm} \cdot Zm \quad (70)$$

The above functions are density-dependent loss terms for processes such as disease (e.g. viruses) and implicit grazing by higher trophic levels that occur at greater rates when plankton are more abundant. Here, density-dependent losses are represented using a hyperbolic function of plankton concentration.

2.3.7 Miscellaneous losses

Since silicic acid is at undersaturated concentrations throughout the modern ocean (Yool and Tyrrell, 2003), the silicon component of diatom phytoplankton is additionally vulnerable to dissolution. This is represented here by a simple linear loss rate, per Mongin et al. (2006). Remineralisation of slow-sinking detrital particles is represented by a similar loss rate, per Fasham et al. (1990).

$$DS_{Pd_{Si}} = Diss \cdot Pd_{Si} \quad (71)$$

$$M_D = \mu_D \cdot D \quad (72)$$

2.3.8 Iron supply and removal

Following the submodel of Dutkiewicz et al. (2005), iron is added to the ocean by aeolian deposition of iron-carrying dust at the surface, and removed throughout by scavenging.

$$F_{atmos} = \text{spatially variable rate} \quad (73)$$

Figure 2 shows a map of annual average iron deposition, and *MEDUSA*'s total iron addition (2.6 Gmol y^{-1}) is approximately the same as that of Dutkiewicz et al. (2005).

$$F_{scavenge} = k_{scav} \cdot F_{free} \quad (74)$$

Scavenging occurs at a fixed linear rate, k_{scav}, throughout the full volume of the ocean, but is assumed to only remove "free" iron, F_{free}.

$$F_{free} = F - F_{ligand} \quad (75)$$

MEDUSA's iron state variable, F, represents total iron, and this is assumed to occur in two fractions: "free", F_{free}; and that bound to organic ligands, F_{ligand} Gledhill and van den Berg (1994). In the ocean, it is estimated that more than 97% of total iron is complexed with ligands Boye et al. (2003).

$$F_{ligand} = L_{total} - L_{free} \quad (76)$$

$$L_{free} = 0.5 \cdot \frac{\left(F_1 + \sqrt{F_2}\right)}{k_{FeL}} \quad (77)$$

$$F_1 = k_{FeL} \cdot (L_{total} - F) - 1 \quad (78)$$

$$F_2 = \max\left(F_1^2 + (4 \cdot k_{FeL} \cdot L_{total}), 0\right) \quad (79)$$

The complexation reactions between iron species and ligands occur rapidly, and it is assumed here that they reach equilibrium in a shorter period than model time-step Rose and Waite (2003). In the equations above, L_{total} is the total ligand concentration of seawater, and is assumed to be globally constant; k_{FeL} is the ligand binding strength. Given these equations and parameters, Fig. 2 shows a diagram of the resulting partition between "free" and bound iron over a range of total iron concentration.

2.3.9 Fast detritus remineralisation terms

The differential equations above include terms for the remineralisation of fast-sinking detrital material. The corresponding terms for the generation of fast–sinking detritus are as follows.

$$T_{\text{N}} = \int_{k=1}^{k=64} \left(\text{D1}_{\text{frac}} \cdot \text{M2}_{\text{pd}}\right) \tag{80}$$

$$T_{\text{Si}} = \int_{k=1}^{k=64} \left(\text{D1}_{\text{frac}} \cdot \text{M2}_{\text{Pd}_{\text{Si}}}\right) \tag{81}$$

The full fast-sinking detritus submodel is described in a later section.

2.4 Parameter values

The Tables 1–4 list model parameters, a brief description of each, and their respective values and units. For ease of use, the ordering of parameters reflects their appearance in the `namelist.trc.sms` file in which they are specified (see Appendix A and accompanying model code).

In addition to the parameters above, *MEDUSA* includes a number of control parameters that allow the model to switch between different functional forms for a small number of processes. These appear in `namelist.trc.sms` and are listed in Table 5.

The parameters associated with the fast–sinking detritus submodel are described in a later section.

3 Detritus

Sinking detrital material occurs in *MEDUSA* in two forms that represent particles of different size and which are modelled in distinct ways.

- Small particles are assumed to sink slowly relative to the model timestep, and their elemental concentration is modelled explicitly as a state variable (detrital nitrogen, D).
- Large particles are assumed to sink quickly relative to the model timestep, and their elemental concentration is implicitly remineralised down the water column (nitrogen, carbon, silicon).

Iron cycle changes associated with the remineralisation of both classes of sinking detrital material are assumed to occur in a strict Redfieldian relationship with those of nitrogen, so neither class includes an explicit consideration of iron concentrations.

3.1 Small particles

Small particles sink down the water column at a prescribed rate and are remineralised to utilisable nutrients at a rate dependent on ambient temperature. This takes the form of Q_{10}-type relationships for the implicitly modelled remineralisation processes (i.e. heterotrophic bacteria are not explicitly modelled), and allows faster recycling of detritus in warm tropical waters to support the microbial loop (Pomeroy, 1974). Small particles are also be consumed by both micro- and mesozooplankton which accelerates the return of nitrogen and iron to utilisable forms.

$$\frac{\partial \text{D}}{\partial t} = \ldots - \underbrace{[M_{\text{D}}]}_{\text{remin}} - \underbrace{\left[w_{\text{g}} \cdot \frac{\partial \text{D}}{\partial z}\right]}_{\text{sinking}} \tag{82}$$

3.2 Large particles

Large particles of detritus can have sinking velocities that cannot be resolved given the time and space scales of the physical models in which ecosystem models are commonly embedded. To resolve this here, large detritus is handled in an implicit fashion. The total quantity of large detritus produced during each timestep is integrated vertically and then instantaneously redistributed and remineralised down the water column. As well as sidestepping issues related to the Courant-Friedrichs-Lewy (CFL) condition, this removes the need for additional (and computationally costly) model tracers. The redistribution and remineralisation of large detrital particles uses a variant of the ballast model of Armstrong et al. (2002). This model divides sinking material into organic and mineral components and assumes that a fraction of the organic material is "protected" from degradation by the mineral material. A full description is given in Sect. 3.2.2.

3.2.1 Total sinking flux

In the case of the nitrogen and silicon cycles, the following terms denote the integrated quantities of these elements.

$$T_{\mathrm{N}} = \int_{k=1}^{k=64} (\mathrm{D1}_{\mathrm{frac}} \cdot \mathrm{M2}_{\mathrm{Pd}}) \tag{83}$$

$$T_{\mathrm{Si}} = \int_{k=1}^{k=64} \left(\mathrm{D1}_{\mathrm{frac}} \cdot \mathrm{M2}_{\mathrm{Pd_{Si}}}\right) + \left(\mathrm{D2}_{\mathrm{frac}} \cdot \mathrm{Gm}_{\mathrm{Pd_{Si}}}\right) \tag{84}$$

Large nitrogenous detritus is derived from fractions of the losses of diatoms and mesozooplankton, $\mathrm{D1}_{\mathrm{frac}}$ and $\mathrm{D2}_{\mathrm{frac}}$ respectively. Since diatom cells are smaller than the mesozooplankton that graze them, $\mathrm{D1}_{\mathrm{frac}}$ is assigned a smaller value than $\mathrm{D2}_{\mathrm{frac}}$ so that a fraction of diatom losses is channelled to small detritus.

Fast detrital silicon is similarly derived from loss processes though, since biogenic silica produced by diatoms is not utilised by zooplankton, one of the sources in *MEDUSA* is the egested remains of diatom cells rather than mesozooplankton mortality. Parameters $\mathrm{D1}_{\mathrm{frac}}$ and $\mathrm{D2}_{\mathrm{frac}}$ are again utilised to control the distribution of losses to fast detritus, though biogenic silicon that is not channelled to fast detritus is returned as dissolved silicic acid since there is no silicon component to small detritus.

As it is not explicitly simulated in the current version of *MEDUSA*, organic carbon is implicitly associated with the sources of large detritus, and is calculated as follows.

$$T_{\mathrm{C}} = \int_{k=1}^{k=64} (\theta_{\mathrm{Pd}} \cdot \mathrm{D1}_{\mathrm{frac}} \cdot \mathrm{M2}_{\mathrm{Pd}}) + (\theta_{\mathrm{Zm}} \cdot \mathrm{D2}_{\mathrm{frac}} \cdot \mathrm{M2}_{\mathrm{Zm}}) \tag{85}$$

A quantitatively important component of sinking particles in the ocean (and one which frames the so-called ballast hypothesis; Armstrong et al., 2002) is the biomineral calcium carbonate ($\mathrm{CaCO_3}$). This is used in the shells of certain types of both phytoplankton and zooplankton, but the factors controlling its production are not fully understood (cf. Hood et al., 2006). Since the current version of *MEDUSA* does not include a complete representation of the carbon cycle, and completely omits ocean alkalinity, calcium carbonate production is modelled as a simple function of organic carbon production (i.e. separate from the processes which contribute organic carbon to fast sinking detritus).

$$T_{\mathrm{CaCO_3}} = \mathrm{fc(latitude)} \cdot ((\mathrm{PP}_{\mathrm{Pn}} \cdot \mathrm{Pn}) + (\mathrm{PP}_{\mathrm{Pd}} \cdot \mathrm{Pd})) \tag{86}$$

Where fc(latitude) is a simple function that relates calcium carbonate production to latitude. Reviewing this relationship, Dunne et al. (2007) found that, on a molar basis, this is approximately 0.09 to 0.10 at the equator, and 0.04 at high latitudes, and that it is systematically lower in the North Atlantic (0.02) than the North Pacific (0.06).

As an aside, another unmodelled component of sinking material is lithogenic material such as wind-borne dust that is picked up from the land and settles into the ocean from the atmosphere. Similarly to the biominerals calcium carbonate and biogenic silicon,

this is proposed to affect export production in the ballast hypothesis (Armstrong et al., 2002). Although the iron component of dust is already included in *MEDUSA* to affect phytoplankton growth, at this point the role of dust in export production is not as yet included.

3.2.2 Ballast model

As noted above, one interpretation concerning the sinking flux of material in the ocean is the ballast hypothesis of Armstrong et al. (2002). This posits that a fraction of the sinking organic material is quantitatively associated with sinking inorganic material (calcium carbonate, biogenic silicon, lithogenic material), and that this provides "protection" for the organic matter, allowing it to penetrate deeper into the water column than might be expected from remineralisation rates. Armstrong et al. (2002) originally treated the hypothesis in rather theoretical terms, but it was subsequently parameterised by Klaas and Archer (2002) in a study that synthesised a global dataset of sediment trap measurements. This latter study has subsequently been used as the basis for other work, and its implementation within the model of Dunne et al. (2007) is that adopted here.

Given the total fluxes of organic carbon and ballast minerals in the large detritus class, the ballast model first calculates the fraction of organic carbon that is "protected" by the minerals. The remainder, known as "excess" (and initially the majority), is subject to remineralisation, typically in an exponential manner similar to that proposed by Martin et al. (1987). Since the minerals themselves are subject to dissolution as the particle flux descends through the water column, the amount of organic carbon that can be "protected" also falls, although this occurs at a considerably slower rate than that at which the "excess" is remineralised. As a result, implementing the ballast scheme is done level-by-level down the modelled water column to account for the gradual differential attenuation of the components of the sinking flux.

The fluxes of sinking biogenic silica, $\mathrm{LD}_{\mathrm{Si}}$, and calcium carbonate, $\mathrm{LD}_{\mathrm{CaCO_3}}$, attenuate with depth irrespective of organic carbon.

$$\mathrm{LD}_{\mathrm{Si}}(z) = T_{\mathrm{Si}} \cdot \exp\left(-\frac{z}{d_{\mathrm{Si}}}\right) \tag{87}$$

$$\mathrm{LD}_{\mathrm{CaCO_3}}(z) = T_{\mathrm{CaCO_3}} \cdot \exp\left(-\frac{z}{d_{\mathrm{CaCO_3}}}\right) \tag{88}$$

The fate of organic carbon (and nitrogen and iron; assumed here to remineralise with the same length scale as carbon) must be calculated instead for each level. Total sinking organic carbon, LC, is divided into that protected by ballast, $\mathrm{LC}_{\mathrm{bSi}}$ and $\mathrm{LC}_{\mathrm{bCaCO_3}}$, and "excess" carbon that is available for remineralisation, $\mathrm{LCR}_{\mathrm{e}}$.

$$\mathrm{LC}_{\mathrm{bSi}}(z) = \mathrm{LD}_{\mathrm{Si}}(z) \cdot \frac{M_{\mathrm{Si}}}{M_{\mathrm{org}}} \cdot f_{\mathrm{Si}} \tag{89}$$

$$\mathrm{LC}_{\mathrm{bCaCO_3}}(z) = \mathrm{LD}_{\mathrm{CaCO_3}}(z) \cdot \frac{M_{\mathrm{CaCO_3}}}{M_{\mathrm{org}}} \cdot f_{\mathrm{CaCO_3}} \tag{90}$$

$$\mathrm{LC}_{\mathrm{e}}(z) = \mathrm{LC}(z) - \mathrm{LC}_{\mathrm{bSi}}(z) - \mathrm{LC}_{\mathrm{bCa}}(z) \tag{91}$$

Where M_{Si} and $M_{\mathrm{CaCO_3}}$ convert molar silicon and calcium carbonate ballast into mass equivalents that can then be used with mass-based organic carbon protection ratios f_{Si} and $f_{\mathrm{CaCO_3}}$. The "excess" fraction is attenuated in a similar fashion to the ballast, but with a shorter length scale and the requirement that it is recalculated in each model level to include formerly protected organic carbon that is now (through mineral dissolution) available to the "excess" pool.

Figure 3 shows idealised results from this model, and in the left panel compares these to the classic empirical model derived by Martin et al. (1987):

$$F_{\mathrm{C}}(z) = F_{\mathrm{C}}(100) \cdot \left(\frac{z}{100}\right)^{-0.858} \tag{92}$$

In the upper 300 m of the water column, both models show similar fractional declines in sinking organic carbon, with approximately 40% of the 100 m flux surviving to this depth. Generally, the Dunne et al. (2007) model exhibits greater remineralisation, such that by 1000 m it estimates an organic carbon sinking flux less than one third of that of Martin et al. (1987). The right panel shows the decline of the biominerals with depth. Because of a longer dissolution length scale, a greater proportion of calcium carbonate reaches the seafloor than that of biogenic silicon (relative to the fluxes at 100 m). Also, while silicic acid is present at undersaturated concentrations throughout the water column and so biogenic silicon dissolves at all depths, calcium carbonate is saturated in shallower waters and only dissolves when it becomes undersaturated at greater depths. The saturation horizon used in Fig. 3 is 2700 m, the global average depth calculated from World Ocean Atlas and GLODAP sources, and the ballasting fraction of calcium carbonate only begins to attenuate below this depth. Figure 4 shows the global distribution of this saturation horizon. The geographical pattern occurs because deep water masses gradually accumulate DIC as they transit along the ocean's thermohaline circulation. This material is provided by the biological pump, and its influence gradually shifts the balance of DIC speciation in seawater towards lower carbonate ion (CO_3^{2-}) concentrations. "Young", recently ventilated waters, such as those in the North Atlantic, have accumulated the least material, and CO_3^{2-} concentrations are supersaturated for most of the water column. By contrast, "old" waters that have been isolated from the atmosphere for centuries or more, such as those in the North Pacific, have accumulated the most material, and CO_3^{2-} concentrations are largely undersaturated.

The parameters used in this implementation of the Dunne et al. (2007) model are listed in Table 6.

3.2.3 Alternative models

Although the ballast model has been selected for use here, it is only one of a number of competing models that describe the attenuation of sinking particulate organic material in the ocean, and there is still considerable observational uncertainty concerning export

production (e.g. Buesseler et al., 2007). Alternative models include variants of the original Martin et al. (1987) formulation (e.g. Parekh et al., 2005), models that consider the size spectra of sinking material (e.g. Kriest and Evans, 1999), and those that explicitly include the aggregation of sinking particles (e.g. Burd and Jackson, 2009). Furthermore, the particular parameterisation of the ballast model employed here is also only one among a number of subtly different variants. Alternatives include those of Moore et al. (2004) and Oka et al. (2008).

However, at the present time there is still considerable uncertainty surrounding water column remineralisation (e.g. Buesseler et al., 2007), and the most appropriate choice of export production model is unclear. To this end, the ballast model has been favoured for *MEDUSA* largely because of its relative simplicity, and because of its intrinsic connection with the silicon cycle.

4 Default simulation

The following section describes a simulation and evaluation of *MEDUSA* using the default equations, functional forms and parameter values described previously.

4.1 Physical model

The underlying physical model used in this simulation is version 3.2 of NEMO (Madec, 2008). This is comprised of an ocean general circulation model, OPA9 (Madec et al., 1998; Madec, 2008), coupled with a sea-ice model, Louvain-la-Neuve Ice Model version 2 (LIM2; Timmermann et al., 2005). This physical framework is configured at approximately $1^\circ \times 1^\circ$ horizontal resolution (292×362 grid points), with a focusing of resolution around the equator to improve the representation of equatorial upwelling. Vertical space is divided into 64 levels, which increase in thickness with depth, from approximately 6 m at the surface to 250 m at 6000 m. To improve the representation of deep water circulation, partial level thicknesses are used in the specification of bottom topography.

The model is forced at the ocean surface using DFS4.1 fields developed by the European DRAKKAR collaboration (DRAKKAR Group, 2007). DFS combines elements from two sources: the CORE forcing dataset (Large and Yeager, 2004), from which precipitation and downward short- and long-wave radiation are extracted; and the ERA40 reanalysis, from which 10 m wind and 2 m air temperature and humidity are extracted. The latter fields are used in conjunction with the bulk formulae proposed by Large and Yeager (2004) to compute air/sea and air/sea-ice energy and freshwater fluxes. The frequency of DFS4.1 is monthly for precipitation, daily for radiation and 6-hourly for the turbulent variables. Climatological monthly runoff (Dai and Trenberth, 2002) is applied along the coastline of the land mask.

The sea-ice submodel used here, LIM2, is based upon viscous-plastic ice rheology (Hibler, 1979) and three layer (two layers of sea-ice, one layer of snow) thermodynamics (Semtner, 1976), with a number of updated physical processes (see Timmermann et al., 2005; and references therein). Model sea-ice is coupled to the ocean every 5 ocean timesteps through the non-linear quadratic drag law of the shear between sea-ice and ocean surface velocity (Timmermann et al., 2005). Freshwater exchange between the ocean and sea-ice is calculated from precipitation and ice formation/melting (Fichefet and Morales Maqueda, 1997), where sea-ice salinity is assumed to be 4 psu and rain/snow are assumed fresh. The heat flux between the sea-ice and ocean is proportional to the departure in temperature from salinity-dependent freezing point and the friction velocity at the ice-ocean interface. Solar radiation can penetrate sea-ice not covered by snow, and is dissipated by brine pockets within the ice where it increases latent heat storage (Fichefet and Morales Maqueda, 1997).

Temperature and salinity fields are initialised here from a monthly climatology that combines the World Ocean Atlas climatology with the PHC2.1 database (Steele et al., 2001; high latitudes) and the Medatlas climatology (Jourdan et al., 1998; Mediterranean Sea). To prevent unacceptable drifts in salinity caused by deficiencies in freshwater forcing, sea surface salinity is relaxed towards monthly mean climatology values. The relaxation timescale is 180 days for the open ocean, and 12 days under

sea-ice. Further details concerning model configuration can be found in Barnier et al. (2006), Penduff et al. (2007) and Penduff et al. (2010), but note that these describe higher resolution instances of NEMO.

4.2 Spinup and simulation

Before *MEDUSA* was added to NEMO, a short, physics-only simulation was performed to provide a "moving" ocean circulation field into which the biogeochemistry could be added. The physical model was simulated from rest from the beginning of the forcing dataset (1 January 1958) for a period of 8 years (to 31 December 1965). This period is insufficient for the thermohaline circulation to be fully established, but it is long enough for strong transient behaviour to decline. In early tests with *MEDUSA*, it was found that the model's behaviour was broadly similar between simulations initialised with physical states that had experienced significantly different spin-up periods.

After this initial phase, *MEDUSA* was coupled to the resulting physical state and the simulation was integrated a further 40 years (to 31 December 2005). For this latter phase, *MEDUSA* was initialised using the World Ocean Atlas climatology for dissolved inorganic nitrogen and silicic acid concentrations, and using an iron field derived from a long-duration simulation of a lower resolution GCM (Parekh et al., 2005; Dutkiewicz et al., 2005). All other model tracers were initialised to arbitrary small values.

In addition to the biogeochemical dynamics described previously, the concentrations of dissolved inorganic nitrogen and silicic acid were relaxed towards World Ocean Atlas climatology values in grid cells within 100 km of land. This was done to emulate the input of these nutrients to coastal locations by riverine sources. Since there is, as yet, no corresponding climatology for iron, this nutrient was not relaxed anywhere in the ocean.

4.3 Results

In this section, a selection of model results are presented with the aim of providing a brief overview of *MEDUSA*'s performance. In the first instance, model outputs that can be compared to observational fields are presented. These are followed by Taylor diagrams that aim to more comprehensively evaluate performance (cf. space and time). Next, model fields of interesting but unmeasured (or unmeasureable) properties are shown to illuminate notable aspects of *MEDUSA*. Finally, some plots of the time-evolution of modelled nutrients are shown to illustrate *MEDUSA*'s stability and drift.

Regarding observational fields, these comprise the World Ocean Atlas 2005 nutrients (Garcia et al., 2006), SeaWiFS chlorophyll (O'Reilly et al., 1998) and estimated primary production. The latter is represented here by three empirical models: the VGPM (Behrenfeld and Falkowski, 1997), Eppley-VGPM (Carr et al., 2006) and CbPM (Westberry et al., 2008) productivity models. Three models are included since each predicts quite different productivity from the same chlorophyll input. The observational fields of chlorophyll and productivity used here represent averages over the same 5 year period from 2000 to 2004 inclusive, and this same period is used throughout the following analysis as a standard interval.

Figures 5 and 6 compare *MEDUSA*'s performance in representing, respectively, surface concentrations of the macronutrients DIN and silicic acid. In both cases *MEDUSA* shows similar patterns of agreement (and disagreement). The seasonal patterns of high northern latitudes are well resolved, but nutrients are noticeably lower in equatorial upwelling regions, while significantly higher in the Southern Ocean. This latter discrepancy is particularly marked in the case of silicic acid.

Figure 7 compares *MEDUSA*'s simulated total chlorophyll (non-diatom plus diatom) to corresponding SeaWiFS fields. Note that a logarithmic colour scale is used to best represent the large range in ocean colour. Not uncommonly for ocean models, *MEDUSA*'s representation of chlorophyll exhibits significant discrepancies with observations. *MEDUSA* shows much less pronounced seasonality, spatial boundaries

that are significantly more sharply defined and consistently lower "background" chlorophyll concentrations in the ocean gyres. While the latter regions are not productive areas of the ocean, they represent a significant fraction of its total area. Part of the reason for the model-data mismatches in this area may lie with the assumption of geographically invariant nutrient kinetics, which prevents model phytoplankton from adapting to oligotrophic conditions. In the real world, nutrient uptake kinetics are more plastic, thereby permitting higher concentrations and productivity in the gyres (e.g. Smith et al., 2009).

Figures 8 and 9 compare *MEDUSA*'s simulated total primary production (non-diatom plus diatom) to the estimates of the VGPM, Eppley-VGPM and CbPM models. While *MEDUSA* does not show strong correlations with any of the estimates, the estimates do not strongly correlate with one another either. However, *MEDUSA* does still show systematic differences with the estimates. These include: consistently low subtropical gyre productivity; and elevated productivity in iron-limited regions including the Southern Ocean, equatorial Pacific and (seasonally) North Pacific. In terms of total oceanic primary production (and averaging over the final 10 years of the simulation), *MEDUSA* predicts 50.0 $\mathrm{Gt\,C\,y^{-1}}$, a value within the broad range of the observational estimates, 58.8, 60.4 and 46.3 $\mathrm{Gt\,C\,y^{-1}}$ respectively.

Figures 10–15 show the corresponding model-observational comparisons using Taylor diagrams. These illustrate both the correlation between (circumference axis) and relative variability (radial axis) of model and observations. For each comparison two plots are shown. The first uses annually average fields, but separates the analysis between ocean regions; the second uses globally average fields, but separates the analysis between months. In all cases, model-observation is greater the closer plotted data are to the red/black bullseye on the horizontal axis.

Best agreement occurs for *MEDUSA*'s nutrient fields, particularly those of dissolved inorganic nitrogen. While there remains sigificant scatter, *MEDUSA* generally shows good correlation with World Ocean Atlas 2005 fields, and comparable magnitudes of variability. This agreement is very weak in the case of chlorophyll, where the model

both correlates poorly and shows much less variability that the observed SeaWiFS fields. Although estimated productivity is based on the same SeaWiFS chlorophyll fields, *MEDUSA*'s agreement with the three productivity models is actually greater. The CbPM model agrees best, although correlations are still relatively weak.

Figures 16–23 show model properties of relevance to *MEDUSA*'s structure, but for which there is little or no observational information.

Figure 16 illustrates the difference in seasonality in the populations of diatom and non-diatom phytoplankton. The former show strongly seasonal behaviour, with high bloom concentrations in spring-summer and near-absence in winter. While the latter also show seasonality, it is considerably more modulated, with small but significant populations during the winter.

Unsurprisingly, this pattern is repeated in Fig. 17, which shows the separate primary production of both groups. Integrating, the diatoms are responsible for 17.0% of total primary production in *MEDUSA*. Estimates of this fraction in the real world are not common. Several estimates for specific locations exist and range from 13 to 34% (Nelson and Brzezinski, 1997; Blain et al., 1997; Brzezinski et al., 1998), though these estimates do not cover the full range of ocean ecosystems. Global estimates are rarer, though a survey by Mann (1999) suggested 40 to 45%, greater than that from the local studies, and much greater than that estimated by *MEDUSA*.

Although diatom primary production appears at the low end of literature estimates, biogenic opal production by *MEDUSA* slightly higher than that estimated. Figure 19 shows the global distribution of opal production, which largely follows diatom production, though areas such as the North Pacific and Southern Ocean show elevated production because of higher Si:N ratios (see Fig. 18). Globally integrated opal production is 262.6 $\mathrm{Tmol\,Si\,y^{-1}}$, 9% higher than the 240 $\mathrm{Tmol\,Si\,y^{-1}}$ estimated by Trégueret al. (1995).

Figure 19 also shows the split between primary production in the mixed layer and that deeper in the water column. The fraction is greatest at high latitudes in both summer and (especially) winter. Lower latitudes show much lower fractions especially

in the oligotrophic subtropical gyres where nutrients are permanently limiting. Globally, 69.6% of primary production occurs in the mixed layer. Following up on nutrient limitation, Fig. 21 shows annual average limitations for both phytoplankton. Averaging spatially, non-diatoms are slightly more limited by iron (0.575) than nitrogen (0.628). Diatoms are most limited by iron (0.407), followed by silicon (0.518) then nitrogen (0.559).

Largely following the availability of their favoured prey, Fig. 20 shows the seasonal distributions of micro- and mesozooplankton. The former closely matches the availability of the small, non-diatom phytoplankton. However, although the mesozooplankton have a preference for microzooplankton equal to diatoms, their distribution closely resembles diatoms, with generally low concentrations elevated wherever diatoms are blooming. However, while the diatoms are the smaller fraction of the phytoplankton community, their grazers make up 55.5% of total surface zooplankton.

Another size-based aspect of *MEDUSA* lies in slow- and fast-sinking detritus. Figure 22 shows the production of both classes of detritus. Unsurprisingly, given *MEDUSA*'s foodweb, the distribution of slow-sinking detritus largely resembles that of the the smaller scale portion of the ecosystem, while fast-sinking detritus follows diatoms and mesozooplankton. In terms of production, 74.9% of detrital particles are small but, as Fig. 23 shows, by 100 m the total sinking flux has fallen to 24.3% of the 33.9 $\mathrm{Gt\,C\,y^{-1}}$ produced, of which only 33.5% is made up of small particles.

Figures 24–26 show the time evolution of regionally averaged nutrient profiles across the whole simulated period. These are plotted to quantify the scale of vertical nutrient redistribution that occurs during *MEDUSA* simulations, and to assess the extent to which the model has equilibriated by the end of the simulated period. Since the resupply of surface nutrients is dependent on vertical gradients, changes in these wrought by the model can be very important.

Of the two macronutrients, nitrogen and silicon, profiles change only slightly during the simulation. The most striking changes occur in the Southern Ocean where both

show strong shifts in the vertical gradients of nutrient concentration. As already seen in the fields shown in Figs. 5 and 6, surface concentrations in this region increase significantly relative to the World Ocean Atlas. By the end of the simulation these rises have slowed significantly, but they suggest a systematic problem with either physical or biogeochemical fluxes in this ocean region.

In the case of iron, in which the initial condition is from model output rather than an observational climatology, any changes that occur in basin profiles are less clearly erroneous. A general pattern is for iron concentrations to fall slightly in the surface 100 m within the first decade of simulation, and then to stabilise to a repeating annual cycle afterwards. This quick equilibriation is unsurprising, since surface iron concentrations are strongly controlled by aeolian deposition and biological activity. However, below around 1000 m iron concentrations are clearly drifting slowly downwards on a much longer time-scale. This difference between the iron and the nitrogen cycles is initially surprising, since the former is largely slaved to the latter, though it stems in part from the inclusion of iron scavenging, a biogeochemical pathway that has no analogue in the nitrogen cycle. Some iron cycle models stop scavenging below a fixed concentration (e.g. Aumont et al., 2003), while others tie it to the concentration of biological particles (e.g. Moore et al., 2004; Galbraith et al., 2010) both of which would act to decrease the deep drift found in *MEDUSA*. However, other studies also use lower resolution GCMs and much longer spin-up periods (4000 y, Aumont et al., 2003; 3000 y, Dutkiewicz et al., 2005; 3000 y, Moore and Doney, 2007; 1000 y, Galbraith et al., 2010), and the drift in *MEDUSA* may simply stem from the short spin-up used in this study.

Finally, Fig. 27 complements earlier results by showing globally averaged time-series of the surface fields that are compared above to observations. The panels illustrate both the monthly variability across the simulation, and the inter-annual trends as it progresses. As already noted, the surface concentrations of both macronutrients show a common pattern of initial rise, followed by a gradual plateauing as their distributions come into equilibrium with physical and biogeochemical fluxes. In contrast,

both surface chlorophyll and primary production are relatively constant, and show no systematic drift. Inter-annual variability occurs, but there is no strong trend to increased or decreased biological activity. Assuming that NEMO's physical behaviour is realistic (which is supported by NEMO's good agreement with observational fields), this suggests that *MEDUSA* has a systematic deficiency that permits the accumulation of nutrients in the surface waters of (largely) the Southern Ocean.

5 Discussion

A significant factor in the adoption of increasingly complex models is the growing awareness of how ongoing anthropogenic changes to the Earth system will impact plankton ecosystems in a disparate number of ways. The most well-known of these changes is the warming of the Earth's climate by the accumulation of the climatically-active gas CO_2 in the atmosphere. This warming has led to a concommitant warming of the (surface) ocean (e.g. Lyman et al., 2010), and it is believed that this will primarily impact plankton systems through changes to surface nutrient concentrations driven by increasing water column stratification (e.g. Bopp et al., 2005). This change in the availability of raw materials for phytoplankton growth is a fundamental one for plankton systems, and is amenable to study using even relatively simplified NPZD models. However, a number of other ongoing changes require more sophisticated treatments of marine ecology. For example, although increasing ocean stratification will lead to decreasing vertical nutrient supply to the surface ocean, not all nutrient species will be affected similarly because of differences in their distributions. Nitrogen and phosphorus nutrients, for instance, are known to covary strongly in a Redfield relationship (Tyrrell, 1999). However, silicic acid is regenerated much deeper in the water column (Yool and Tyrrell, 2003), and is liable to be affected differently by increasing stratification. Since this nutrient plays a crucial role in the ecology of the diatoms, a key phytoplankton group (Mann, 1999) with an important role in export production (Dugdale and Wilkerson, 1998), wider ecosystem functioning is liable to change if the diatoms become disadvantaged.

Similarly, also in part related to the change in surface nutrient conditions, another anticipated impact lies with the occurrence and distribution of nitrogen fixation (Capone et al., 2005). This process is an important source of fixed nitrogen for oligotrophic regions of the surface ocean, and offsets its consumption through denitification (Tyrrell, 1999). A declining supply of physically-supplied fixed nitrogen from depth driven by increasing stratification and, potentially, increasing anoxia-mediated denitrification (cf. Deutsch et al., 2007), may act to shift phytoplankton community structure in favour of groups capable of utilising dissolved dinitrogen gas.

The invasion of the ocean by anthropogenic CO_2 is increasing dissolved inorganic carbon concentrations (Key et al., 2004), and altering the pH of seawater. This process, known as ocean acidification (Caldeira and Wickett, 2003; Orr et al., 2005), is predicted to have a number of different effects on ocean biota (Raven et al., 2005), but a major one will be the increasing solubility of the biomineral calcium carbonate in surface (and deep) waters. Since a large number of planktonic species utilise this mineral for structural purposes, changes in seawater chemistry that accelerate its dissolution are liable have a significant impact.

These latter changes to the ocean system mitigate in favour of ecosystem models that include more sophistication than conventional NPZD models, so that their consequences can be assessed. However, although research has outlined the ecosystem processes described above, there are still large gaps that preclude robust and reliable predictions. For instance, in the case of nitrogen fixation, there are a number of different phylogenetic groups engaged in this process (e.g. cyanobacteria, diatoms, even some metazoans; Kneip et al., 2007), with the result that functional behaviour is diverse and difficult to model within the confines of a single state variable. simply. There are potentially even issues concerning seemingly established ideas about the correlation of nitrogen fixation with warm waters (cf. Le Quéré et al., 2005) that may be incorrect (cf. Monteiro et al., 2010). Similarly, while calcification may be expected to be straightforwardly related to the saturation state of calcium carbonate, experimental and field work has found a wide range of responses that, again, preclude

simple modelling (e.g. Riebesell et al., 2000; Iglesias-Rodriguez et al., 2008).

Within this context, *MEDUSA* aims to expand upon classical NPZD models, while restricting itself to biogeochemical cycles and biological functional groups that are more completely understood (cf. Anderson, 2005; Flynn, 2005). Hence, *MEDUSA*'s incorporation of diatoms and the silicon cycle (cf. Smetacek, 1985; Dugdale and Wilkerson, 1998), and a microbial loop of smaller phytoplankton and zooplankton (cf. Pomeroy, 1974; Azam et al., 1983). However, as noted by Hood et al. (2006), even these expansions are not without uncertainty. The silicon cycle, for instance, ignores the contributions to opal production of both the silicoflagellates and (more significantly) the radiolarians. Furthermore, *MEDUSA* also omits a detailed consideration of internal cell physiology (cf. Flynn, 2001). Nonetheless, the intention of *MEDUSA* is to provide a post-NPZD plankton ecosystem model, with a parameterisation that is robust, and whose major state variables are amenable to analysis and comparison with observational data throughout the global domain.

In general, *MEDUSA*'s performance is acceptable, with global patterns of nutrients and productivity that closely follow those observed. Major features such as oligotrophic gyres and the seasonal progression of plankton blooms and nutrient depletion are reproduced. And at the global scale, *MEDUSA*'s productivity falls well within the range estimated from observations, both in terms of organic carbon and biogenic opal. Furthermore, although indirect, the multi-decadal stability of vertical macronutrient gradients (except in the Southern Ocean; see below) suggests that *MEDUSA*'s export production successfully balances nutrient resupply by physical mechanisms. Drifts in deep iron concentrations suggest an insufficient spin-up period, but surface gradients equilibriate quickly as with the macronutrients. However, there are a number of significant discrepancies between *MEDUSA* and observations that should be noted.

Firstly, *MEDUSA* tends to accumulate nutrients, especially silicic acid, in the surface waters of the Southern Ocean. Since *MEDUSA*'s productivity is similar to that estimated from satellite observations, this tends to suggest that either the export fraction of *MEDUSA* is too low in this region (i.e. the biological pump does not transfer

organic material deep enough), or that NEMO's upwelling is too strong (i.e. excessive quantities of nutrient are upwelled, and cannot be processed by surface biology). Given the good agreement between NEMO and observed physical fields, the former explanation may guide future improvement.

Secondly, the oligotrophic gyres in *MEDUSA* have lower concentrations of chlorophyll and are less productive than observed. Again, this may be the result of either biological or physical deficiencies in the model. For instance, the low nutrient concentrations in these regions may be insufficient to permit even slow growth of *MEDUSA*'s phytoplankton on recycled nutrients. Alternatively, the resolution of NEMO used here may omit mesoscale processes that supply nutrients to the surface ocean (e.g. McGillicuddy et al., 2003). As noted already, the former suggestion is supported by work that permits adaptation of model phytoplankton to oligotrophic conditions (Smith et al., 2009). The latter suggestion may be investigated in future using higher resolution instances of NEMO.

As noted, both of these deficiencies may have biogeochemical roots. At present, *MEDUSA* has not been objectively tuned to more closely match observational fields. Current parameterisation is instead derived from literature values and from subjective "tuning" where parameter values have been found to cause systematic errors. Previous studies have found that the localised optimisation of a biogeochemical model at particular locations can be successful at improving model performance when the model is then simulated in 3-D at large scale (Oschlies and Schartau, 2005). Consequently, objective tuning, coupled to validation in 3-D, may be a future avenue to improve the performance of *MEDUSA* and to diminish the most significant current errors.

A further issue with the simulation of *MEDUSA* examined here is the suggestion that the spin-up period used is insufficient, most clearly apparent in the drift of deep iron concentrations, but also in the more gradual adjustment of DIN and silicic acid distributions. In the specific case of iron, given an initial condition derived from a different model, the operation of iron scavenging throughout the model domain, and the long ventilation timescale of the deep ocean (2000 y; Ostlund and Stuiver, 1980), this is

perhaps unsurprising. The medium resolution used here, as well as the high resolution used in other applications of *MEDUSA* (e.g. Popova et al., 2010), preclude spin-ups of more than a few decades. However, lower resolution instances of the NEMO GCM are available, and future investigation of up–scaled *MEDUSA* output from longer spin–ups of coarser grids may provide one solution to this problem. Nonetheless, and as noted already, despite deep ocean drifts, the biogeochemical cycles of *MEDUSA*'s surface ocean, where most biological activity takes place, reach quasi–equilibrium well within the time–scale of the simulation described here.

In summary, despite the deficiencies noted above, we believe that *MEDUSA* represents a valuable tool for global scale simulations of the plankton ecosystem. One that is intermediate between the simplicity of NPZD models, and the expensive complexity of PFT models, but whose complexity provides a "good fit" with our current ability to validate models at the global scale. Future work with *MEDUSA* will include its application to a range of contemporary topics, including Arctic climate change (Kwok and Rothrock, 2009) and ocean acidification (Orr et al., 2005).

6 Conclusions

- *MEDUSA*, a novel, size–based plankton ecosystem model of the nitrogen, silicon and iron cycles for the global ocean is introduced
- The performance of *MEDUSA* is evaluated using global–scale observational fields following a multi–decadal simulation (1966 to 2005 inclusive).
- *MEDUSA* reliably produces global patterns of surface nutrients and productivity, and (generally) preserves vertical nutrient gradients.
- *MEDUSA*'s major deficiencies are excessive surface nutrients in the Southern Ocean (especially silicic acid), and low productivity in oligotrophic gyres.
- *MEDUSA* estimates that surface productivity is dominated by small plankton, but that the deep biological pump is driven by large plankton.

Appendix A

The following provides a structural outline of the computer code that accompanies this description of *MEDUSA*. This code does not encompass the entire NEMO model, but includes those modules that either include *MEDUSA*'s calculations, or those in which *MEDUSA* makes an appearance for operational reasons.

The *MEDUSA* model is organised in a similar manner to other passive tracer modules in the NEMO model. The majority of the code directly associated with *MEDUSA* is located within the `NEMO/TOP_SRC/MEDUSA` directory, with one minor exception that is described later. The actual model code is distributed across 9 separate routines as follows.

– `par_medusa.F90`
this routine declares the tracer and diagnostic arrays required for *MEDUSA*;

– `sms_medusa.F90`
this routine declares the parameters required for *MEDUSA*;

– `trcctl_medusa.F90`
this routine checks that the correct number of passive tracers is specified;

– `trcini_medusa.F90`
this routine initialises the passive tracers to default values unless they are provided by a restart file;

– `trclsm_medusa.F90`
this routine initialises the parameters to the values specified in `namelist.trc.sms`;

– `trcsms_medusa.F90`
this routine is called by the NEMO model during a simulation and in turn calls the *MEDUSA* routines that calculate biogeochemical sources and sinks;

– `trcopt_medusa.F90`
this routine calculates the submarine light field;

– `trcbio_medusa.F90`
this is the main model routine and includes (almost) all of the ecosystem equations used for the biogeochemical sources and sinks for tracers;

– `trcsed_medusa.F90`
this routine both initialises the aeolian iron deposition and $\Omega_{calcite}$ CCD fields and calculates the sinking of the slow detritus tracer.

Aside from these routines, *MEDUSA* includes a further modification to the passive tracer damping routine, `trcdmp.F90`. In *MEDUSA*, an existing tracer damping subroutine is altered such that dissolved inorganic nitrogen and silicic acid are damped globally but only within 100 km of the coast. This damping relaxes nitrogen and silicon nutrients towards World Ocean Atlas values (Garcia et al., 2006), and aims to emulate the supply of these macronutrients to coastal regions from riverine sources. Since no corresponding climatology exists for the iron micronutrient, its concentrations experience no relaxation anywhere within the model ocean.

Acknowledgements. The authors are grateful to the NEMO development team at NOCS for their technical support of this work. In particular, the assistance of Andrew Coward, Beverly de Cuevas and Steven Alderson has been invaluable in the development and simulation of *MEDUSA*. We are especially indebted to Steven for his patient and thorough detective work that uncovered, and resolved, a serious and cryptic bug deep within NEMO.

The authors gratefully acknowledge the financial support of the Natural Environmental Research Council (NERC). This work was performed as part of Themes 2 and 9 of the NERC Oceans 2025 strategic marine science programme.

References

Anderson, T. R.: Plankton functional type modelling: running before we can walk?, J. Plankton Res., 27, 1073–1081, doi:10.1093/plankt/fbi076, 2005. 1941, 1974

Anderson, T. R.: Progress in marine ecosystem modelling and the "unreasonable effectiveness of mathematics", J. Marine Syst., 81, 4–11, doi:10.1016/j.jmarsys.2009.12.015, 2010. 1941

Anderson, T. R. and Hessen, D. O.: Carbon or nitrogen limitation of marine copepods?, J. Plankton Res., 17, 317–331, 1995. 1944

Anderson, T. R. and Pondaven, P.: Non-redfield carbon and nitrogen cycling in the Sargasso Sea: pelagic imbalances and export flux, Deep-Sea Res. Pt. I, 50, 573–591, 2003. 1944, 1952

Antonov, J. I., Locarnini, R. A., Boyer, T. P., Mishonov, A. V., and Garcia, H. E.: World Ocean Atlas 2005, Volume 2: Salinity, in: NOAA Atlas NESDIS 62, edited by: Levitus, S., US Government Printing Office, Washington, DC, USA, 182 pp., 2006. 1996

Armstrong, R. A., Lee, C., Hedges, J. I., Honjo, S., and Wakeham, S. G.: A new, mechanistic model for organic carbon fluxes in the ocean: based on the quantitative association of POC with ballast minerals, Deep-Sea Res. Pt. II, 49, 219–236, 2002. 1944, 1959, 1960, 1961

Aumont, O., Maier-Reimer, E., Blain, S., and Monfray, P.: An ecosystem model of the global ocean including Fe, Si, P colimitations, Global Biogeochem. Cy., 17, 1060, doi:10.1029/2001GB001745, 2003. 1971

Azam, F., Fenchel, T., Field, J. G., Gray, J. S., Meyer-Reil, L. A., and Thingstad, F.: The Ecological Role of Water-Column Microbes in the Sea, Mar. Ecol.-Prog. Ser., 10, 257–263, 1983 1974

Baird, M. E. and Suthers, I. M.: A size-resolved pelagic ecosystem model, Ecol. Model., 203, 185–203, doi:10.1016/j.ecolmodel.2006.11.025, 2007. 1945

Barnier, B., Madec, G., Penduff, T., et al.: Impact of partial steps and momentum advection schemes in a global ocean circulation model at eddy-permitting resolution, Ocean Dynam., 56, 543–567, doi:10.1007/s10236-006-0082-1, 2006. 1966

Behrenfeld, M. J. and Falkowski, P. G.: Photosynthetic rates derived from satellite-based chlorophyll concentration, Limnol. Oceanogr., 42, 1–20, 1997. 1967

Blain, S., Leynaert, A., Tréguer, P., Chretiennot-Dinet, M. C., and Rodier, M.: Biomass, growth rates and limitation of equatorial Pacific diatoms, Deep-Sea Res. Pt. I, 44, 1255–1275, 1997. 1969

Bopp, L., Aumont, O., Cadule, P., Alvain, S., and Gehlen, M.: Response of diatoms distribution to global warming and potential implications: A global model study, Global Biogeochem. Cy., 32, L19606, doi:10.1029/2005GL023653, 2005. 1972

Boye, M., Aldrich, A. P., van den Berg, C. M. G., de Jong, J. T. M., Veldhuis, M., and de Baar, H. J. W.: Horizontal gradient of the chemical speciation of iron in surface waters of the northeast Atlantic Ocean, Mar. Chem., 80, 129–143, 2003. 1956

Brzezinski, M. A., Villareal, T. A., and Lipschultz, F.: Silica production and the contribution of diatoms to new and primary production in the central North Pacific, Mar. Ecol.-Prog. Ser., 167, 89–104, 1998. 1969

Buesseler, K. O., Lamborg, C. H., Boyd, P. W., et al.: Revisiting Carbon Flux Through the Ocean's Twilight Zone, Science, 316, 567–570, doi:10.1126/science.1137959, 2007. 1964

Burd, A. B. and Jackson, G. A.: Particle aggregation, Annu. Rev. Mar. Sci., 1, 65–90, 2009. 1964

Caldeira, K. and Wickett, M. E.: Anthropogenic carbon and ocean pH, Nature, 425, 365–365, doi:10.1038/425365a, 2003. 1973

Capone, D. G., Burns, J. A., Montoya, J. P., Subramaniam, A., Mahaffey, C., Gunderson, T., Michaels, A. F., and Carpenter, E. J.: Nitrogen fixation by *Trichodesmium* spp.: An important source of new nitrogen to the tropical and subtropical North Atlantic Ocean, Global Biogeochem. Cy., 19, GB2024, doi:10.1029/2004GB002331, 2005. 1973

Carr, M.-E., Friedrichs, M. A. M., Schmeltz, M., et al.: A comparison of global estimates of marine primary production from ocean color, Deep-Sea Res. Pt. II, 53, 741–770, 2006. 1967

Cox, P. M., Betts, R. A., Jones, C. D., Spall, S. A., and Totterdell, I. J.: Acceleration of global warming due to carbon-cycle feedbacks in a coupled climate model, Nature, 408, 184–187, 2000. 1941

Dai, A. and Trenberth, K. E.: Estimates of freshwater discharge from continents: latitudinal and seasonal variations, J. Hydrometeorol., 3, 660–687, 2002. 1965

Deutsch, C., Sarmiento, J. L., Sigman, D. M., Gruber, N., and Dunne, J. P.: Spatial coupling of nitrogen inputs and losses in the ocean, Nature, 445, 163–167, doi:10.1038/nature05392,

2007. 1973
DRAKKAR Group: Eddy-permitting Ocean Circulation Hindcasts of past decades, CLIVAR Exchanges, 42(12), 8–10, 2007. 1965
Dugdale, R. C. and Wilkerson, F. P.: Silicate regulation of new production in the equatorial Pacific upwelling, Nature, 391, 270–273, 1998. 1972, 1974
Dunne, J. P., Sarmiento, J. L., and Gnanadesikan, A.: A synthesis of global particle export from the surface ocean and cycling through the ocean interior and on the seafloor, Global Biogeochem. Cy., 21, GB4006, doi:10.1029/2006GB002907, 2007. 1944, 1960, 1961, 1963, 1995
Dutkiewicz, S., Follows, M. J., and Parekh, P.: Interactions of the iron and phosphorus cycles: A three-dimensional model study, Global Biogeochem. Cy., 19, GB1021, doi:10.1029/2004GB002342, 2005. 1944, 1956, 1966, 1971
Eppley, R. W.: Temperature and phytoplankton growth in the sea, Fish. B.-NOAA, 70, 1063–1085, 1972. 1947
Fasham, M. J. R., Ducklow, H. W., and McKelvie, S. M.: A nitrogen-based model of plankton dynamics in the oceanic mixed layer, J. Mar. Res., 48, 591–639, 1990. 1947, 1951, 1955
Fichefet, T. and Morales Maqueda, M. A.: Sensitivity of a global sea ice model to the treatment of ice thermodynamics and dynamics, J. Geophys. Res., 102, 12609–12646, 1997. 1965
Flynn, K. J.: A mechanistic model for describing dynamic multi-nutrient, light, temperature interactions in phytoplankton, J. Plankton Res., 23, 977–997, 2001. 1974
Flynn, K. J.: Castles built on sand: dysfunctionality in plankton models and the inadequacy of dialogue between biologists and modellers, J. Plankton Res., 27, 1205–1210, 2005. 1941, 1974
Furnas, M. J.: *In situ* growth rates of marine phytoplankton: approaches to measurement, community and species growth rates, J. Plankton Res., 12, 1117–1151, 1990. 1945
Galbraith, E. D., Gnanadesikan, A., Dunne, J. P., and Hiscock, M. R.: Regional impacts of iron-light colimitation in a global biogeochemical model, Biogeosciences, 7, 1043–1064, doi:10.5194/bg-7-1043-2010, 2010. 1944, 1971
Garcia, H. E., Locarnini, R. A., Boyer, T. P., and Antonov, J. I.: World Ocean Atlas 2005, Volume 4: Nutrients (phosphate, nitrate, silicate), in: NOAA Atlas NESDIS 64, edited by: Levitus, S., US Government Printing Office, Washington, DC, USA, 396 pp., 2006. 1967, 1978
Gledhill, M. and van den Berg, C.: Determination of complexation of iron (III) with natural organic complexing ligands in seawater using cathodic stripping voltammetry, Mar. Chem.,

47, 41–54, 1994. 1956
Gregg, W. W., Ginoux, P., Schopf, P. S., and Casey, N. W.: Phytoplankton and iron: validation of a global three-dimensional ocean biogeochemical model, Deep-Sea Res. Pt. II, 50, 3143–3169, 2003. 1941
Gruber, N., Sarmiento, J. L., and Stocker, T. F.: An improved method for detecting anthropogenic CO_2 in the oceans, Global Biogeochem. Cy., 10, 809–837, 1996. 1941
Hibler, W. D.: A dynamic thermodynamic sea ice model, J. Phys. Oceanogr., 9, 815–846, 1979. 1965
Hood, R. R., Laws, E. A., Armstrong, R. A., et al.: Pelagic functional group modeling: Progress, challenges and prospects, Deep-Sea Res. Pt. II, 53, 459–512, 2006. 1941, 1960, 1974
Iglesias-Rodriguez, M. D., Halloran, P. R., Rickaby, R. E. M., et al.: Phytoplankton Calcification in a High-CO_2 World, Science, 320, 336–340, doi:10.1126/science.1154122, 2008. 1974
Jourdan, D., Balopoulos, E., Garcia-Fernandez, M.-J., and Maillard, C.: Objective analysis of temperature and salinity historical data set over the Mediterranean basin, OCEANS '98 Conference Proceedings, 1, 82–87, doi:10.1109/OCEANS.1998.725649, 1998. 1965
Key, R. M., Kozyr, A., Sabine, C. L., et al.: A global ocean carbon climatology: Results from Global Data Analysis Project (GLODAP), Global Biogeochem. Cy., 18, GB4031, doi:10.1029/2004GB002247, 2004. 1973, 1996
Klaas, C. and Archer, D.: Association of sinking organic matter with various types of mineral ballast in the deep sea: Implications for the rain ratio, Global Biogeochem. Cy., 16, 1116, doi:10.1029/2001GB001765, 2002. 1961
Kneip, C., Lockhart, P., Voß, C., and Maier, U.: Nitrogen fixation in eukaryotes – New models for symbiosis, BMC Evol. Biol., 7, 55, doi:10.1186/1471-2148-7-55, 2007. 1973
Kriest, I. and Evans, G. T.: Representing phytoplankton aggregates in biogeochemical models, Deep-Sea Res. Pt. I, 46, 1841–1859, 1999. 1964
Kwok, R. and Rothrock, D. A.: Decline in Arctic sea ice thickness from submarine and ICESat records: 1958–2008, Geophys. Res. Lett., 36, L15501, doi:10.1029/2009GL039035, 2009. 1976
Large, W. and Yeager, S.: Diurnal to decadal global forcing for ocean and sea-ice models: the data sets and flux climatologies, CGD Division of the National Center for Atmospheric Research, NCAR Technical Note: NCAR/TN-460+STR, 2004. 1965
Le Quéré, C., Harrison, S. P., Prentice, C., et al.: Ecosystem dynamics based on plankton functional types for global ocean biogeochemistry models, Glob. Change Biol., 11, 2016–

2040, 2005. 1941, 1943, 1973
Locarnini, R. A., Mishonov, A. V., Antonov, J. I., Boyer, T. P., and Garcia, H. E.: World Ocean Atlas 2005, Volume 1: Temperature, in: NOAA Atlas NESDIS 61, edited by: Levitus, S., US Government Printing Office, Washington, DC, USA, 182 pp., 2006. 1996
Lyman, J. M., Good, S. A., Gouretski, V. V., Ishii, M., Johnson, G. C., Palmer, M. D., Smith, D. M., and Willis, J. K.: Robust warming of the global upper ocean, Nature, 465, 334–337, doi:10.1038/nature09043, 2010. 1972
Madec, G., Delecluse, P., Imbard, M., and Lévy, C.: OPA 8.1 ocean general circulation model reference manual, Note du Pole de modélisation, Institut Pierre Simon Laplace, France, Technical Report 11, 91 pp., 1998. 1964
Madec, G.: NEMO reference manual, ocean dynamic component: NEMO-OPA, Note du Pole de modélisation, Institut Pierre Simon Laplace, Technical Report 27, Note du Pôle de modélisation, Institut Pierre Simmon Laplace, France, No. 27, ISSN No. 1288–1619, 2008. 1942, 1964
Mann, D. G.: The species concept in diatoms, Phycologia, 38, 437–495, 1999. 1945, 1969, 1972
Martin, J. H., Knauer, G. A., Karl, D. M., and Broenkow, W. W.: VERTEX: Carbon cycling in the northeastern Pacific, Deep-Sea Res. Pt. I, 34, 267–285, 1987. 1961, 1962, 1963, 1964, 1995
Martin-Jézéquel, V., Hildebrand, M., and Brzezinski, M. A.: Silicon metabolism in diatoms: implications for growth, J. Phycol., 36, 821–840, 2000. 1950
McGillicuddy, D. J., Anderson, L. A., Doney, S. C., and Maltrud, M. A.: Eddy-driven sources and sinks of nutrients in the upper ocean: Results from a 0.1° resolution model of the North Atlantic, Global Biogeochem. Cy., 17, 1035, doi:10.1029/2002GB001987, 2003. 1975
Mongin, M., Nelson, D. M., Pondaven, P., and Tréguer, P.: Simulation of upper-ocean biogeochemistry with a flexible-composition phytoplankton model: C, N and Si cycling and Fe limitation in the Southern Ocean, Deep-Sea Res. Pt. II, 53, 601–619, 2006. 1944, 1949, 1955
Monteiro, F. M., Follows, M. J., and Dutkiewicz, S.: Distribution of diverse nitrogen fixers in the global ocean, Global Biogeochem. Cycles, 24, GB3017, doi:10.1029/2009GB003731, 2010. 1973
Moore, J. K., Doney, S. C., and Lindsay, K.: Upper ocean ecosystem dynamics and iron cycling in a global three-dimensional model, Global Biogeochem. Cy., 18, GB4028,

doi:10.1029/2004GB002220, 2004. 1941, 1943, 1964, 1971
Moore, J. K. and Doney, S. C.: Iron availability limits the ocean nitrogen inventory stabilizing feedbacks between marine denitrification and nitrogen fixation, Global Biogeochem. Cy., 21, GB2001, doi:10.1029/2006GB002762, 2007. 1971
Nelson, D. M. and Brzezinski, M. A.: Diatom growth and productivity in an oligotrophic mid-ocean gyre: a 3-year record from the Sargasso Sea near Bermuda, Limnol. Oceanogr., 42, 473–486, 1997. 1969
O'Reilly, J. E., Maritorena, S., Mitchell, B. G., Siegal, D. A., Carder, K. L., Garver, S. A., Kahru, M., and McClain, C.: Ocean color chlorophyll algorithms for SeaWiFS, J. Geophys. Res., 103, 24937–24953, 1998. 1967
Oka, A., Kato, S., and Hasumi, H.: Evaluating effect of ballast mineral on deep-ocean nutrient concentration by using an ocean general circulation model, Global Biogeochem. Cy., 22, GB3004, doi:10.1029/2007GB003067, 2008. 1964
Orr, J. C., Fabry, V. J., Aumont, O., et al.: Anthropogenic ocean acidification over the twenty-first century and its impact on calcifying organisms, Nature, 437, 681–686, 2005. 1973, 1976
Oschlies, A. and Schartau, M.: Basin-scale performance of a locally optimized marine ecosystem model, J. Mar. Res., 63, 335–358, doi:10.1357/0022240053693680, 2005. 1975
Östlund, G. and Stuiver, M.: GEOSECS Pacific radiocarbon. Radiocarbon, 22, 25–53, 1980. 1975
Palmer, J. R. and Totterdell, I. J.: Production and export in a global ocean ecosystem model, Deep-Sea Res., 48, 1169–1198, 2001. 1941, 1943
Parekh, P., Follows, M. J., and Boyle, E. A.: Decoupling of iron and phosphate in the global ocean, Global Biogeochem. Cy., 19, GB2020, doi:10.1029/ 2004GB002280, 2005. 1944, 1964, 1966
Penduff, T., Le Sommer, J., Barnier, B., Treguier, A.-M., Molines, J.-M., and Madec, G.: Influence of numerical schemes on current-topography interactions in 1/4° global ocean simulations, Ocean Sci., 3, 509–524, doi:10.5194/os-3-509-2007, 2007. 1966
Penduff, T., Juza, M., Brodeau, L., Smith, G. C., Barnier, B., Molines, J.-M., Treguier, A.-M., and Madec, G.: Impact of global ocean model resolution on sea-level variability with emphasis on interannual time scales, Ocean Sci., 6, 269–284, doi:10.5194/os-6-269-2010, 2010. 1966
Pomeroy, L. R.: The Ocean's Food Web, a Changing Paradigm, Bioscience 24, 499–504, 1974. 1958, 1974
Popova, E. E., Coward, A. C., Nurser, G. A., de Cuevas, B., Fasham, M. J. R., and Anderson, T.

R.: Mechanisms controlling primary and new production in a global ecosystem model - Part I: Validation of the biological simulation, Ocean Sci., 2, 249–266, doi:10.5194/os-2-249-2006, 2006. 1947

Popova, E. E., Yool, A., Coward, A. C., Aksenov, Y. K., Alderson, S. G., de Cuevas, B. A., and Anderson, T. R.: Control of primary production in the Arctic by nutrients and light: insights from a high resolution ocean general circulation model, Biogeosciences Discuss., 7, 5557–5620, doi:10.5194/bgd-7-5557-2010, 2010. 1976

Raven, J. A. and Falkowski, P. G.: Oceanic sinks for atmospheric CO_2, Plant Cell Environ., 22, 741–755, 1999. 1940

Raven, J. A., Caldeira, K., Elderfield, H., et al.: Ocean acidification due to increasing atmospheric carbon dioxide, Royal Society of London, UK, 2005. 1973

Redfield, A. C.: On the proportions of organic derivatives in seawater and their relation to the composition of plankton, in: James Johnstone Memorial Volume, edited by: Daniel, R. J., University of Liverpool, UK, 176–192, 1934. 1943

Riebesell, U., Zondervan, I., Rost, B., Tortell, P. D., Zeebe, R. E., and Morel, F. M. M.: Reduced calcification of marine plankton in response to increased atmospheric CO_2, Nature, 407, 364–367, doi:10.1038/35030078, 2000. 1974

Rose, A. L. and Waite, T. D.: Kinetics of iron complexation by dissolved natural organic matter in coastal waters, Mar. Chem., 84, 85–103, 2003. 1957

Sarmiento, J. L., Slater, R. D., Fasham, M. J. R., Ducklow, H. W., Toggweiler, J. R., and Evans, G. T.: A seasonal three-dimensional ecosystem model of nitrogen cycling in the North Atlantic euphotic zone, Global Biogeochem. Cy., 7, 417–450, 1993. 1941

Schmittner, A., Oschlies, A., Giraud, X., Eby, M., and Simmons, H. L.: A global model of the marine ecosystem for long-term simulations: Sensitivity to ocean mixing, buoyancy forcing, particle sinking, and dissolved organic matter cycling, Global Biogeochem. Cy., 19, GB3004, doi:10.1029/2004GB002283, 2005.

Semtner, A. J.: A model for the thermodynamic growth of sea ice in numerical investigation of climate, J. Phys. Oceanogr., 6, 376–389, 1976. 1965

Six, K. D. and Maier-Reimer, E.: Effects of plankton dynamics on seasonal carbon fluxes in an ocean general circulation model, Global Biogeochem. Cy., 10, 559–583, 1996. 1941, 1943

Smetacek, V. S.: Role of sinking in diatom life–history cycles : ecological, evolutionary and geological significance, Mar. Biol., 84, 239–251, 1985. 1974

Smith, S. L., Yamanaka, Y., Pahlow, M., and Oschlies, A.: Optimal uptake kinetics: physiological

acclimation explains the pattern of nitrate uptake by phytoplankton in the ocean, Mar. Ecol.-Prog. Ser., 384, 1–12, doi:10.3354/meps08022, 2009. 1968, 1975

Steele, M., Morley, R., and Ermold, W.: PHC: a global ocean hydrography with a high quality Artic Ocean, J. Climate, 14, 2079–2087. 1965

Taylor, A. H., Geider, R. J., and Gilbert, F. J. H.: Seasonal and latitudinal dependencies of phytoplankton carbon-to-chlorophyll a ratios: results of a modelling study, Mar. Ecol.-Prog. Ser., 152, 51–66, 1997. 1947, 1951

Timmermann, R., Goosse, H., Madec, G., Fichefet, T., Ethe, C., and Duliere, V.: On the representation of high latitude processes in the ORCA-LIM global coupled sea ice–ocean model, Ocean Model., 8, 175–201, doi:10.1016/j.ocemod.2003.12.009, 2005. 1964, 1965

Tréguer, P., Nelson, D. M., Van Bennekom, A. J., DeMaster, D. J., Leynaert, A. and Quéguiner, B.: The silica balance in the world ocean: a reestimate, Science, 268, 375–379, 1995. 1969

Tyrrell, T.: The relative influences of nitrogen and phosphorus on oceanic primary production, Nature, 400, 525–531, 1999. 1972, 1973

Westberry, T., Behrenfeld, M. J., Siegel, D. A., and Boss, E.: Carbon-based primary productivity modeling with vertically resolved photoacclimation, Global Biogeochem. Cy., 22, GB2024, doi:10.1029/2007GB003078, 2008. 1967

Yool, A. and Tyrrell, T.: The role of diatoms in regulating the ocean's silicon cycle, Global Biogeochem. Cy., 17, 1103, doi:10.1029/2002GB002018, 2003. 1955, 1972

Yool, A., Oschlies, A., Nurser, A. J. G., and Gruber, N.: A model-based assessment of the TrOCA approach for estimating anthropogenic carbon in the ocean, Biogeosciences, 7, 723–751, doi:10.5194/bg-7-723-2010, 2010. 1947

Zeebe, R. E. and Wolf-Gladrow, D. A.: CO_2 in Seawater: Equilibrium, Kinetics, Isotopes, Elsevier, Amsterdam, Netherlands, 2001. 1996

Table 1. Phytoplankton growth parameters.

ξ	Chl:N conversion factor (Redfield ratio of 6.625) g chl $(\text{mol N})^{-1}$	0.0256
α_{Pn}, α_{Pd}	chl-specific initial slope of P-I curve g C $(\text{g chl})^{-1}$ $(\text{W m}^{-2})^{-1}$ d^{-1}	10.0, 7.5
V_{Pn}, V_{Pd}	maximum phytoplankton growth rate d^{-1}	0.53, 0.50
$\theta^{\text{Chl}}_{\text{max, Pn}}$, $\theta^{\text{Chl}}_{\text{max, Pd}}$	maximum chl:C ratio g chl $(\text{g C})^{-1}$	0.10, 0.10
$R^0_{\text{Si:N}}$	minimum diatom Si:N ratio mol Si $(\text{mol N})^{-1}$	0.2
$R^0_{\text{N:Si}}$	minimum diatom N:Si ratio mol N $(\text{mol Si})^{-1}$	0.2
U_∞	hypothetical growth ratio at ∞ Si:N ratio –	1.5
$k_{\text{N, Pn}}$, $k_{\text{N, Pd}}$	N nutrient uptake half-saturation constants mmol N m^{-3}	0.50, 0.75
k_{Si}	Si nutrient uptake half-saturation constant mmol Si m^{-3}	0.75
$k_{\text{Fe, Pn}}$, $k_{\text{Fe, Pd}}$	Fe nutrient uptake half-saturation constants µmol Fe m^{-3}	0.33, 0.67

Table 2. Zooplankton grazing parameters.

g_μ, g_{m}	maximum zooplankton grazing rate d^{-1}	2.0, 0.5
k_μ, k_{m}	zooplankton grazing half-saturation constants mmol N m^{-3}	0.8, 0.3
ϕ	zooplankton grazing inefficiency –	0.20
β_{N}	zooplankton N assimilation efficiency –	0.69
β_{C}	zooplankton C assimilation efficiency –	0.69
k_{C}	zooplankton net C growth efficiency –	0.80
$p_{\mu\text{Pn}}$, $p_{\mu\text{D}}$	microzooplankton grazing preferences –	0.75, 0.25
p_{mPn}, p_{mPd}, $p_{\text{mz}\mu}$, p_{mD}	mesozooplankton grazing preferences –	0.15, 0.35, 0.35, 0.15

Discussion Paper | Discussion Paper | Discussion Paper | Discussion Paper |

Table 3. Plankton and detritus loss parameters.

$\mu_{1,\mathrm{Pn}}$, $\mu_{1,\mathrm{Pd}}$	phytoplankton loss rates d^{-1}	0.02, 0.02
$\mu_{1,\mathrm{z\mu}}$, $\mu_{1,\mathrm{Zm}}$	zooplankton loss rates d^{-1}	0.02, 0.02
$\mu_{2,\mathrm{Pn}}$, $\mu_{2,\mathrm{Pd}}$	phytoplankton maximum loss rates d^{-1}	0.1, 0.1
$k_{\mathrm{z\mu}}$, k_{Zm}	phytoplankton loss half-saturation constants mmol N m^{-3}	0.5, 0.5
$\mu_{2,\mathrm{z\mu}}$, $\mu_{2,\mathrm{Zm}}$	zooplankton maximum loss rates d^{-1}	0.5, 0.75
$k_{\mathrm{z\mu}}$, k_{Zm}	zooplankton loss half-saturation constants mmol N m^{-3}	0.2, 0.75
μ_{D}	detrital N remineralisation rate d^{-1}	0.016

Table 4. Miscellaneous parameters.

θ_{Pn}, θ_{Pd}	phytoplankton C:N ratio mol C $(\mathrm{mol\,N})^{-1}$	6.625
$\theta_{\mathrm{z\mu}}$, θ_{Zm}	zooplankton C:N ratio mol C $(\mathrm{mol\,N})^{-1}$	6.625
θ_{D}	detritus C:N ratio mol C $(\mathrm{mol\,N})^{-1}$	6.625
R_{Fe}	phytoplankton Fe:N uptake ratio µmol Fe $(\mathrm{mol\,N})^{-1}$m	30.0
L_{total}	total ligand concentration µmol m^{-3}	1.0
k_{FeL}	dissociation constant for (Fe + ligand)	100.0
k_{scav}	scavenging rate of "free" Fe d^{-1}	0.001
Diss	diatom frustule dissolution rate d^{-1}	0.006
w_{g}	detrital sinking rate m d^{-1}	2.5

Table 5. *MEDUSA* switches.

`jphy`	switches phytoplankton maximum growth between temperature independence (= 0) and dependence (= 1); the default is `jphy` = 1
`jmpn`	switches non-diatom phytoplankton density-dependent mortality between linear (= 1), quadratic (= 2), hyperbolic (= 3) and sigmoid (= 4) forms; the default is `jmpn` = 3
`jmpd`	as `jmpn` but for diatom phytoplankton
`jmzmi`	as `jmpn` but for microzooplankton
`jmzme`	as `jmpn` but for mesozooplankton
`jmd`	as `jphy` but for detrital remineralisation; the default is `jmd` = 1

Table 6. Fast detritus submodel parameters.

$D1_{frac}$	fast detritus fraction of diatom losses –	0.25
$D1_{frac}$	fast detritus fraction of mesozooplankton losses –	1.00
fc(90°)	polar calcium carbonate:organic C fraction mol $CaCO_3$ (mol C)$^{-1}$	0.02
fc(0°)	equatorial calcium carbonate:organic C fraction mol $CaCO_3$ (mol C)$^{-1}$	0.10
M_{org}	organic carbon mass:mole ratio, C g (mol C)$^{-1}$	12.011
M_{CaCO_3}	calcium carbonate mass:mole ratio, $CaCO_3$ g (mol C)$^{-1}$	100.086
M_{Si}	biogenic Si mass:mole ratio, SiO_2 g (mol Si)$^{-1}$	60.084
f_{CaCO_3}	calcium carbonate protection ratio g C (g C)$^{-1}$	0.070
f_{Si}	biogenic Si protection ratio g C (g Si)$^{-1}$	0.026
d_{excess}	excess organic carbon dissolution length scale m	188
d_{CaCO_3}	calcium carbonate dissolution length scale m	3500
d_{Si}	biogenic Si dissolution length scale m	2000

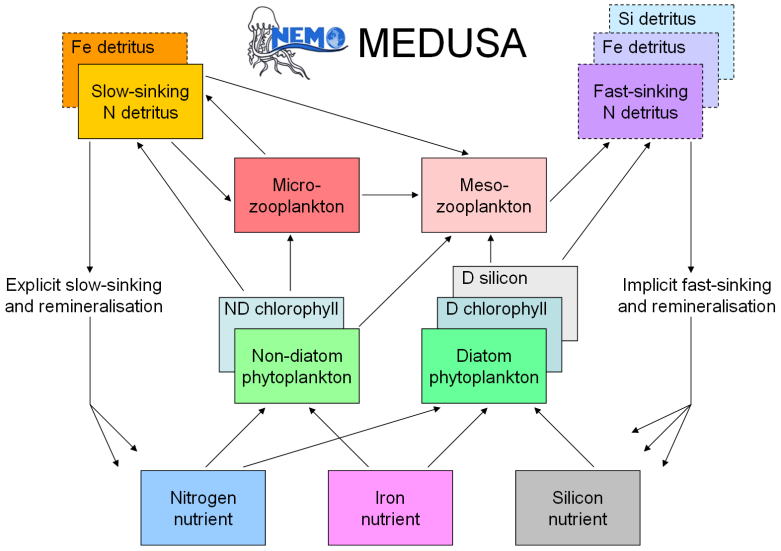

Fig. 1. Schematic diagram of the components and interactions in the *MEDUSA* model. Boxes with solid borders indicate explicitly modelled state variables, while boxes with dashed borders indicate implicitly modelled components. Overlapping boxes indicate components for which multiple currencies are modelled (e.g. different elements, chlorophyll).

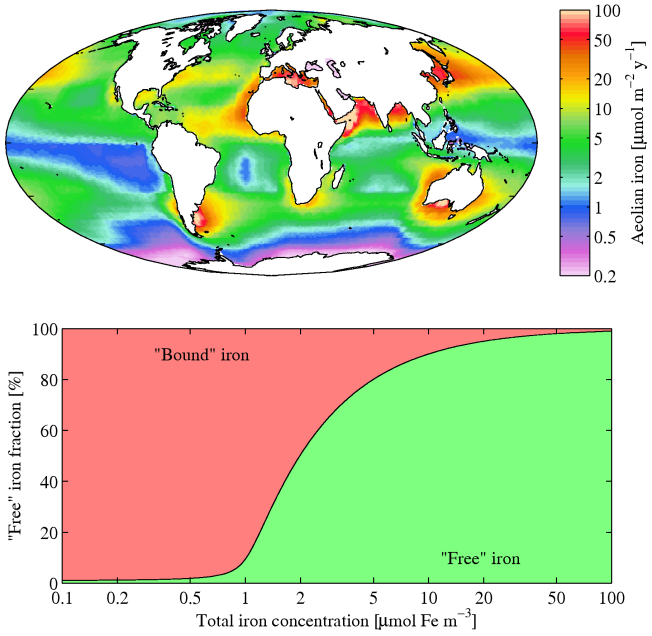

Fig. 2. The top panel shows mean annual aeolian iron input to the ocean (i.e. the quantity of iron that dissolves into seawater from deposited dust). The input is shown on a logarithmic scale in units of µmol m^{-2} y^{-1}, and integrated input is 2.564 Gmol Fe y^{-1}. The bottom panel shows the fractionation of total iron between "free" and ligand-bound forms across a logarithmic range of total iron concentrations.

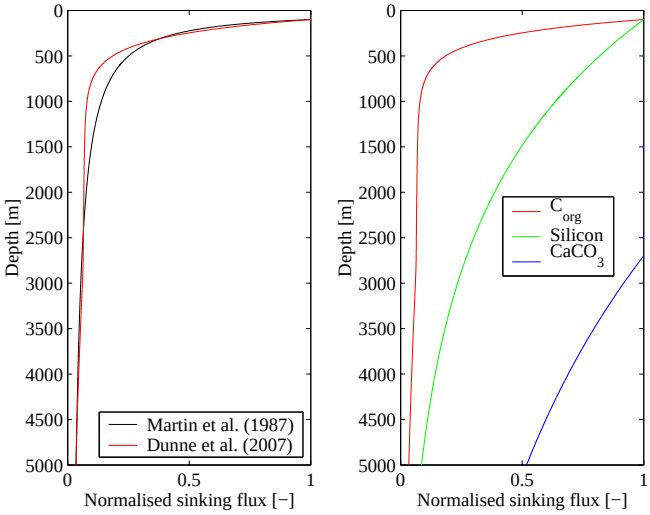

Fig. 3. Vertical attenuation of the sinking flux. The left panel compares the Dunne et al. (2007; red) parameterisation for organic carbon with that of Martin et al. (1987; black). The right panel shows the attenuation of organic carbon (red), biogenic silicon (green) and calcium carbonate (blue). In all cases, fluxes are normalised to those at 100 m.

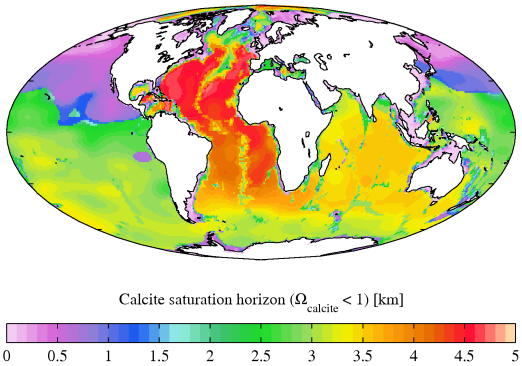

Fig. 4. The global distribution of the depth of the calcite saturation horizon. This is calculated as the shallowest depth at which $\Omega_{calcite}$ is less than 1. The three dimensional field of $\Omega_{calcite}$ is calculated using the CSYS package (Zeebe and Wolf-Gladrow, 2001) together with fields of ocean properties from the World Ocean Atlas (Locarnini et al., 2006; Antonov et al., 2006; temperature and salinity) and GLODAP (Key et al., 2004; DIC and alkalinity) climatologies. Interpolation has been used to fill gaps in the GLODAP climatology including the Arctic, Caribbean, Mediterranean seas and the Malay Archipelago.

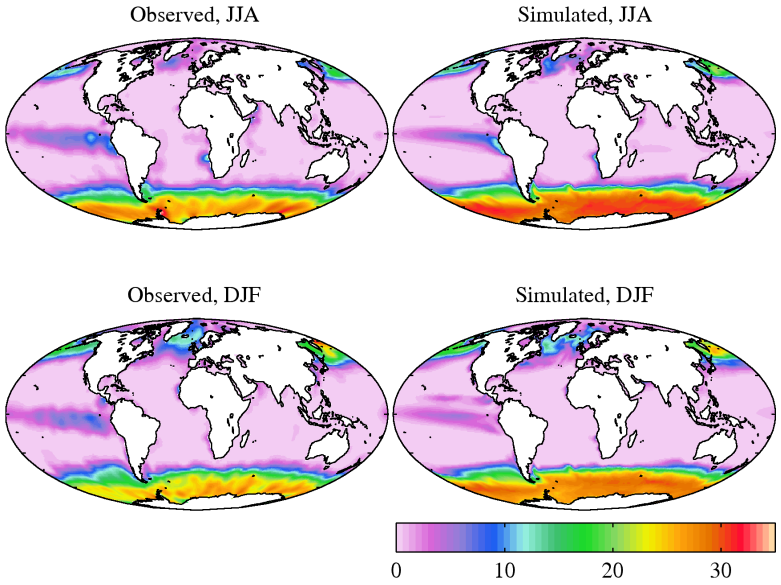

Fig. 5. Observational (World Ocean Atlas, 2005; left) and simulated (right) surface dissolved inorganic nitrogen for northern summer (June-July-August; top) and northern winter (December-January-February; bottom). Concentrations in mmol m^{-3}.

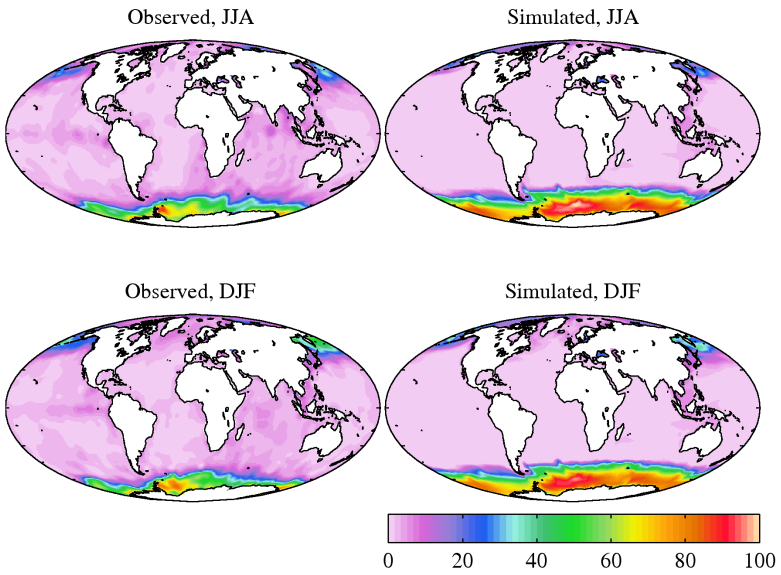

Fig. 6. Observational (World Ocean Atlas, 2005; left) and simulated (right) surface silicic acid for northern summer (June-July-August; top) and northern winter (December-January-February; bottom). Concentrations in mmol m^{-3}.

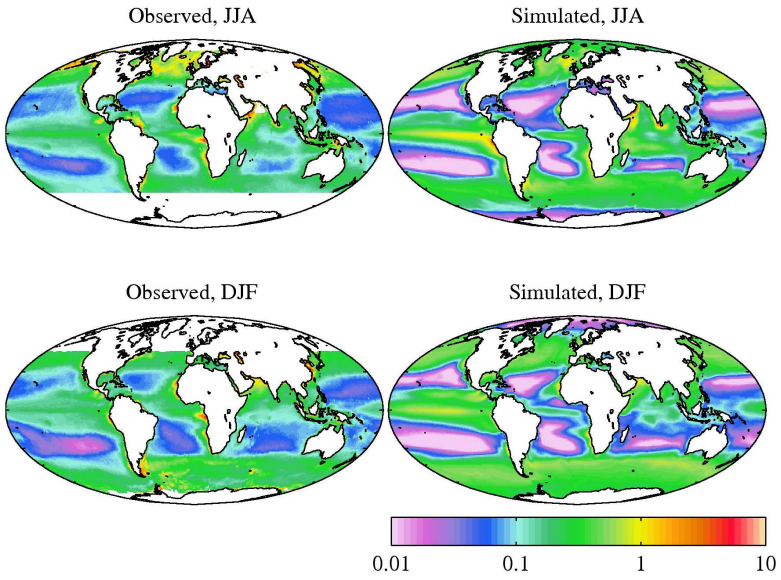

Fig. 7. Observational (SeaWiFS ; left) and simulated (right) surface chlorophyll for northern summer (June-July-August; top) and northern winter (December-January-February; bottom). Concentrations in mg chl m^{-3}.

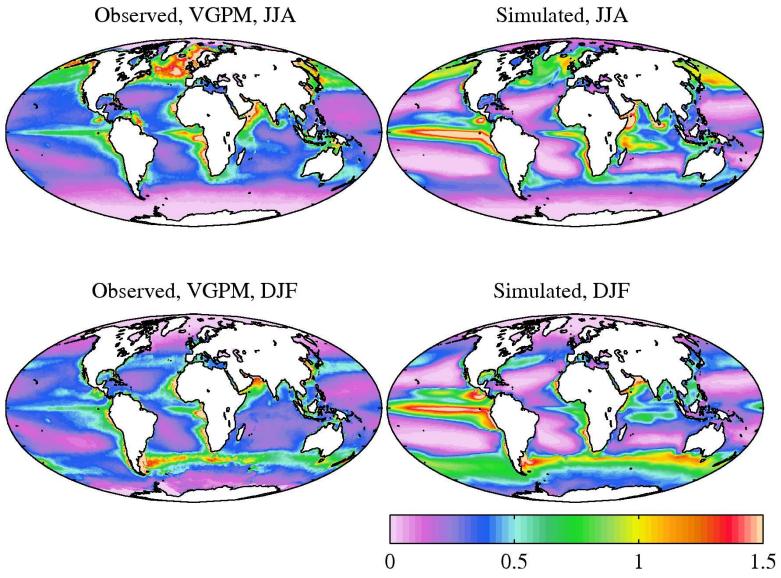

Fig. 8. Observational (VGPM model; left) and simulated (right) integrated primary production for northern summer (June-July-August; top) and northern winter (December-January-February; bottom). The observational field here is estimated using the VGPM model and SeaWiFS chlorophyll observations. Production in g C m^{-2} d^{-1}.

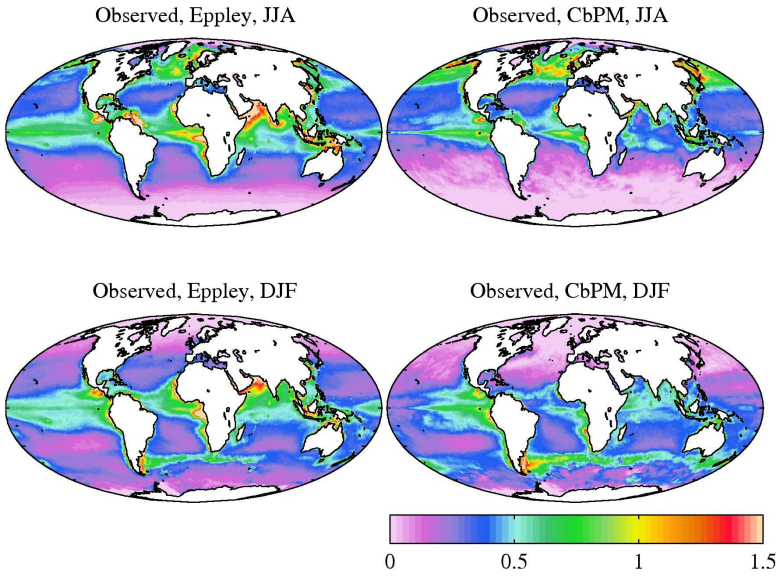

Fig. 9. Observational integrated primary production as per Fig. 8 but for the Eppley-VGPM (left) and CbPM (right) models. Production in g C m^{-2} d^{-1}.

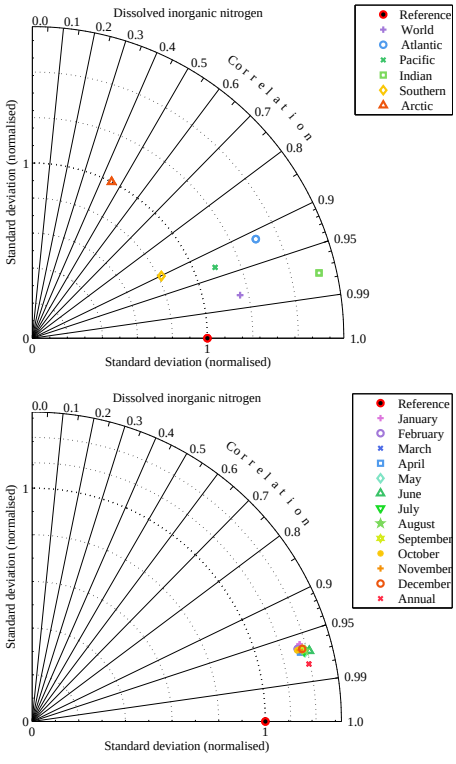

Fig. 10. Taylor diagrams of spatial (top) and temporal (bottom) model-observation comparisons for surface dissolved inorganic nitrogen. In the upper panel, simulated annual means for different regions are compared to corresponding observational fields. In the lower panel, simulated global average means for different months are compared to corresponding observational fields.

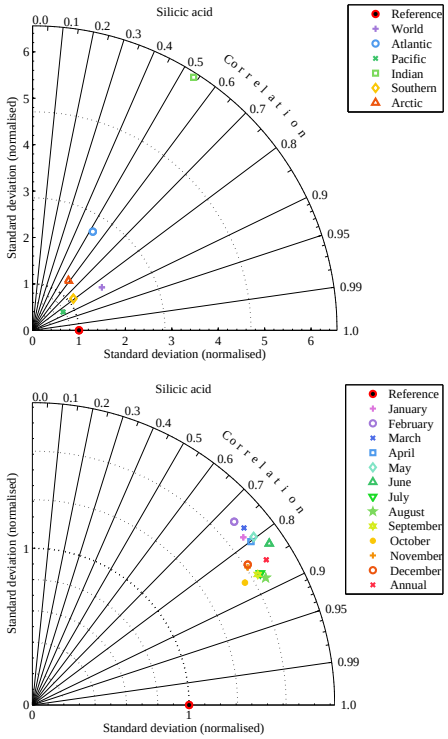

Fig. 11. Taylor diagrams of spatial (top) and temporal (bottom) model-observation comparisons for surface silicic acid. In the upper panel, simulated annual means for different regions are compared to corresponding observational fields. In the lower panel, simulated global average means for different months are compared to corresponding observational fields.

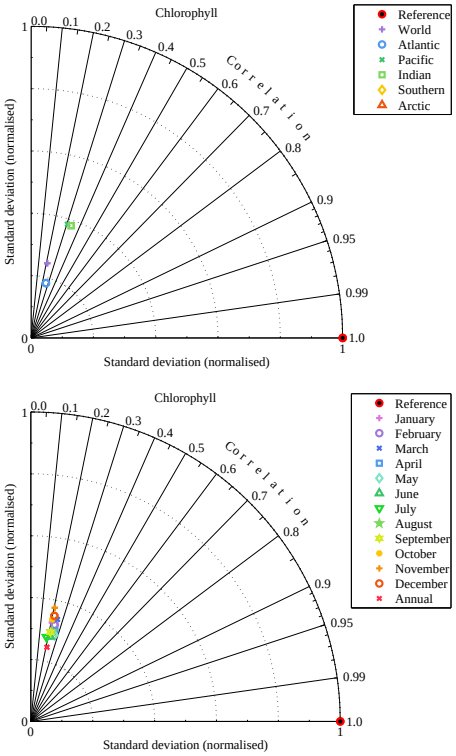

Fig. 12. Taylor diagrams of spatial (top) and temporal (bottom) model-observation comparisons for surface chlorophyll. In the upper panel, simulated annual means for different regions are compared to corresponding observational fields. In the lower panel, simulated global average means for different months are compared to corresponding observational fields.

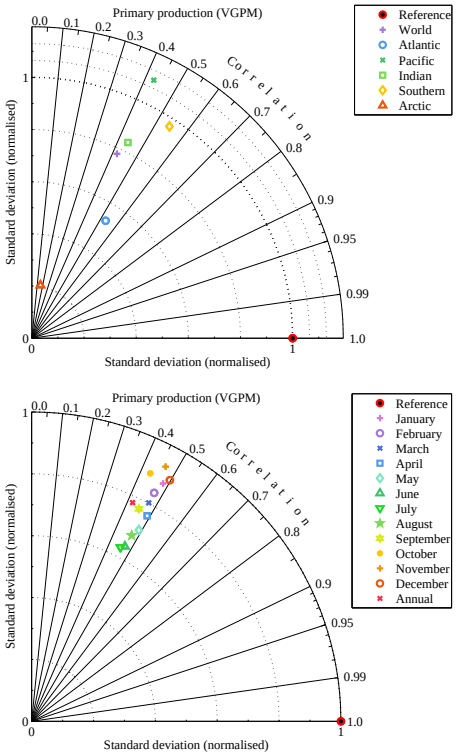

Fig. 13. Taylor diagrams of spatial (top) and temporal (bottom) model-observation comparisons for integrated primary production (VGPM estimated). In the upper panel, simulated annual means for different regions are compared to corresponding observational fields. In the lower panel, simulated global average means for different months are compared to corresponding observational fields.

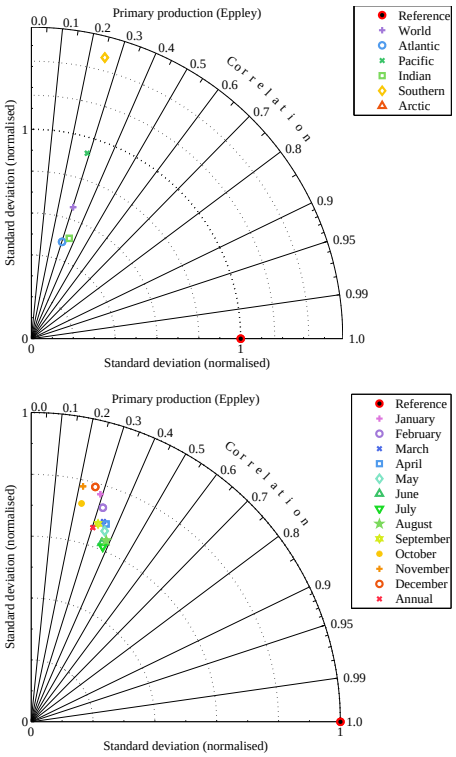

Fig. 14. Taylor diagrams of spatial (top) and temporal (bottom) model-observation comparisons for integrated primary production (Eppley-VGPM estimated). In the upper panel, simulated annual means for different regions are compared to corresponding observational fields. In the lower panel, simulated global average means for different months are compared to corresponding observational fields.

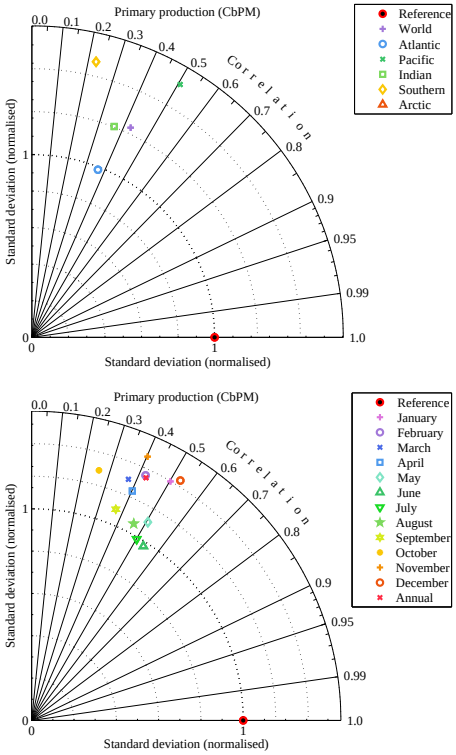

Fig. 15. Taylor diagrams of spatial (top) and temporal (bottom) model-observation comparisons for integrated primary production (CbPM estimated). In the upper panel, simulated annual means for different regions are compared to corresponding observational fields. In the lower panel, simulated global average means for different months are compared to corresponding observational fields.

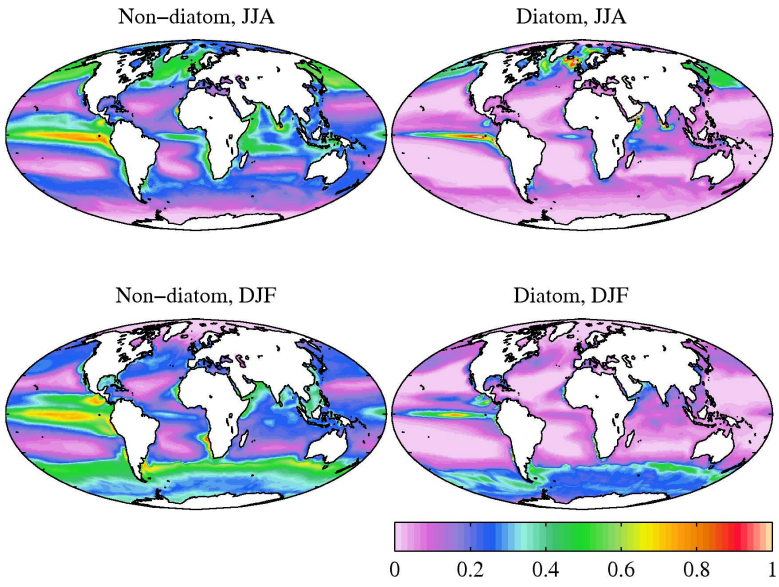

Fig. 16. Simulated surface non-diatom phytoplankton (left) and diatom phytoplankton (right) concentrations for northern summer (June-July-August; top) and northern winter (December-January-February; bottom). Concentrations in mmol m^{-3}.

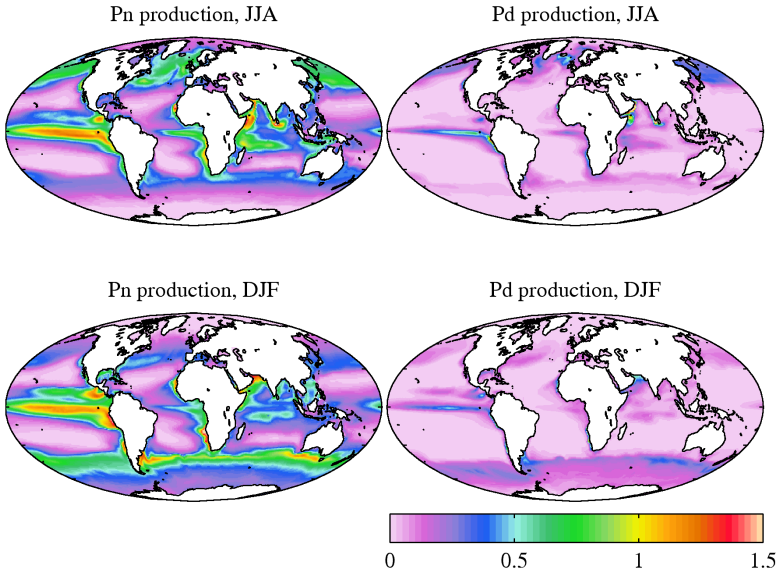

Fig. 17. Simulated non-diatom (left) and diatom (right) primary production for northern summer (June-July-August; top) and northern winter (December-January-February; bottom). Production in g C m^{-2} d^{-1}.

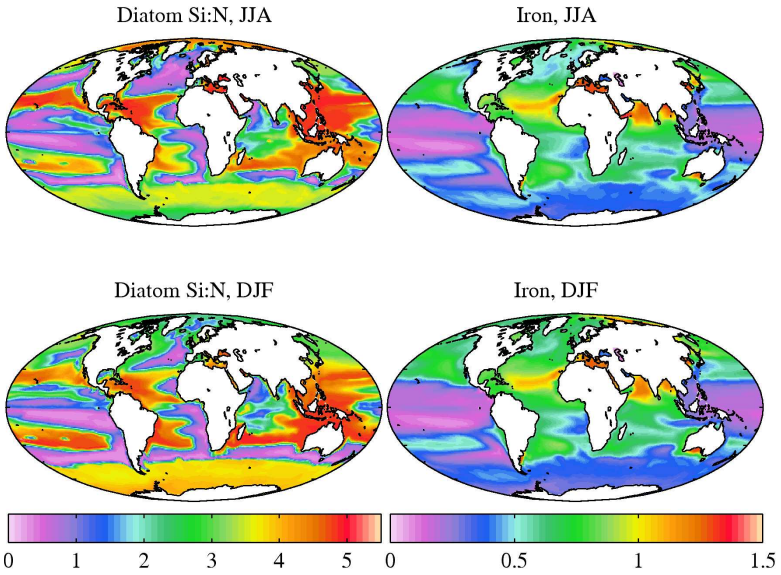

Fig. 18. Simulated surface diatom phytoplankton Si:N ratio (left) and iron concentration (right) for northern summer (June-July-August; top) and northern winter (December-January-February; bottom). Ratio in mol Si (mol N)$^{-1}$; concentration in µmol m^{-3} .

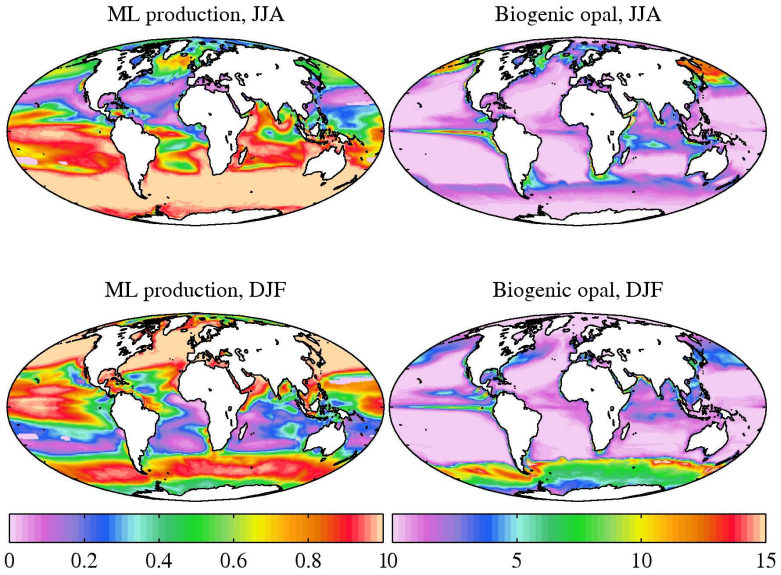

Fig. 19. Simulated mixed layer primary production fraction (left) and diatom biogenic opal production (right) for northern summer (June-July-August; top) and northern winter (December-January-February; bottom). Production fraction is unitless; biogenic opal production in mmol Si m^{-2} d^{-1}.

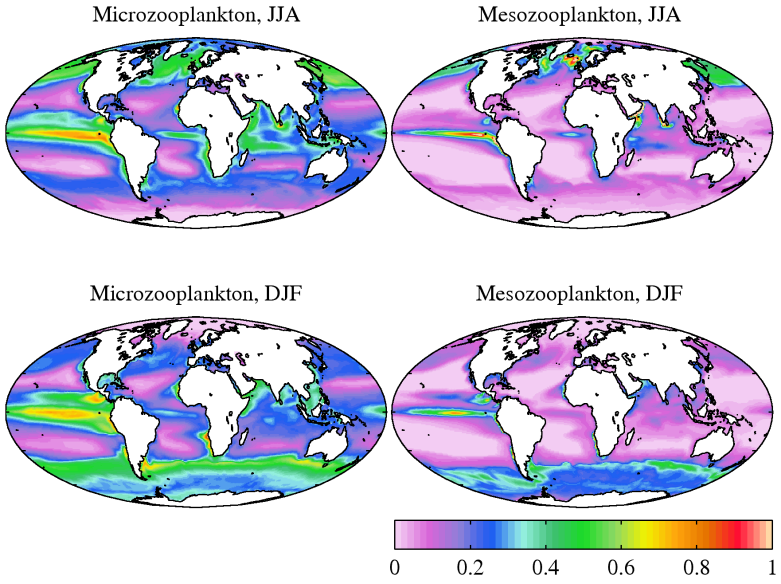

Fig. 20. Simulated surface microzooplankton (left) and mesozooplankton (right) concentrations for northern summer (June-July-August; top) and northern winter (December-January-February; bottom). Concentrations in mmol m^{-3}.

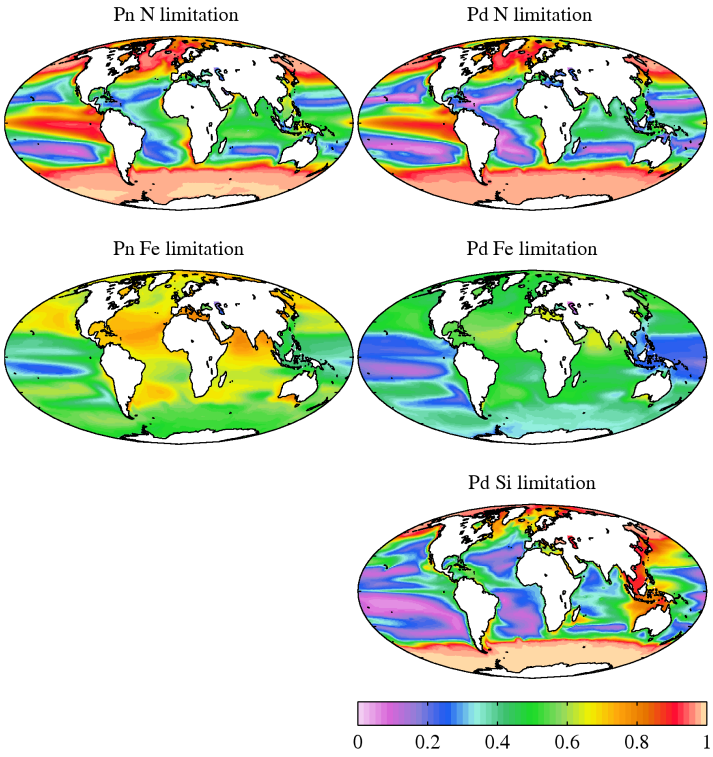

Fig. 21. Simulated annual average non-diatom (left) and diatom (right) limitation factors for nitrogen (top), iron (middle) and silicon (bottom) nutrients. Limitation is weighted by biomass and integrated for the full water column. Limition is unitless.

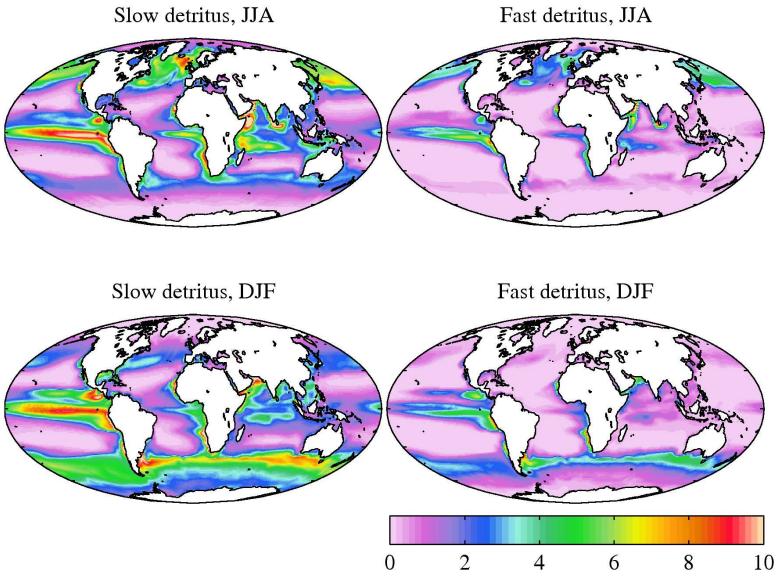

Fig. 22. Simulated slow (left) and fast (right) detritus production for northern summer (June-July-August; top) and northern winter (December-January-February; bottom). Detritus production in mmol N m^{-2} d^{-1}.

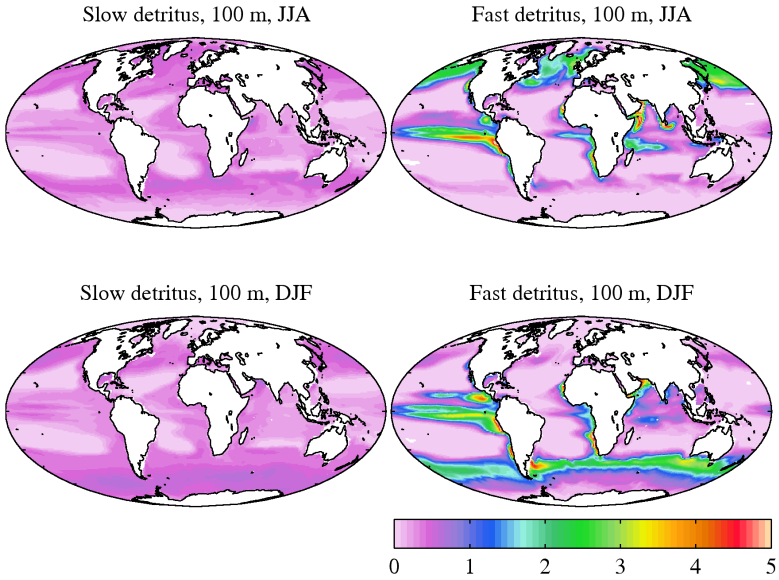

Fig. 23. Simulated slow (left) and fast (right) detrital sinking fluxes at 100 m for northern summer (June-July-August; top) and northern winter (December-January-February; bottom). Detritus production in mmol N m^{-2} d^{-1}.

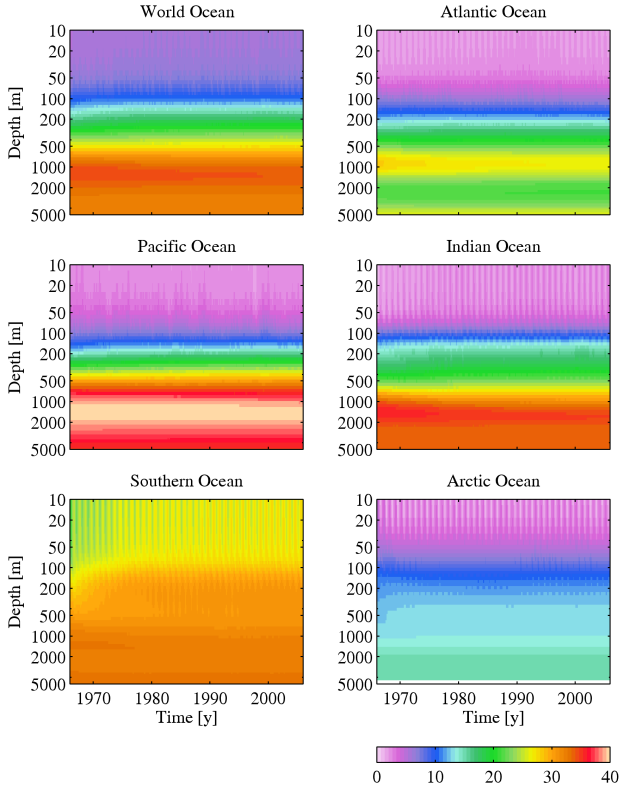

Fig. 24. Simulated vertical profiles of dissolved inorganic nitrogen concentration averaged for the World Ocean (top left) and 5 major regions. Concentrations in mmol N m^{-3}. Note that depth is shown on a logarithmic scale.

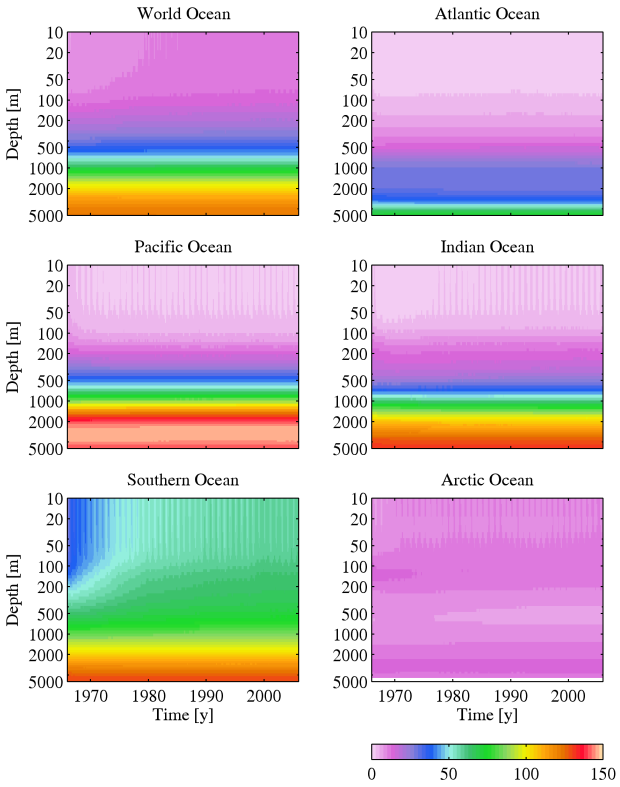

Fig. 25. Simulated vertical profiles of silicic acid concentration averaged for the World Ocean (top left) and 5 major regions. Concentrations in mmol Si m^{-3}. Note that depth is shown on a logarithmic scale.

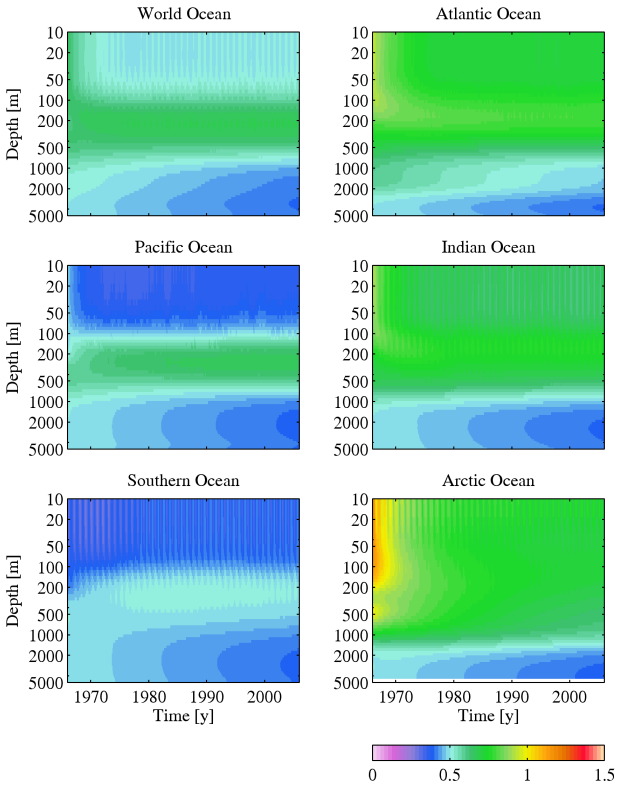

Fig. 26. Simulated vertical profiles of iron concentration averaged for the World Ocean (top left) and 5 major regions. Concentrations in µmol Fe m^{-3}. Note that depth is shown on a logarithmic scale.

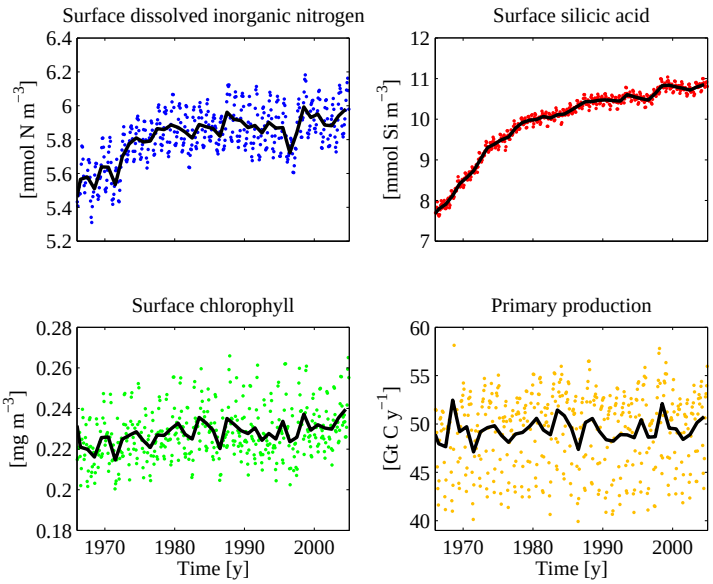

Fig. 27. Globally averaged surface dissolved inorganic nitrogen (top left), surface silicic acid (top right), surface chlorophyll (bottom left) and integrated primary production (bottom right). Solid black lines are annual averages/integral; individual points are individual months. Note that individual monthly primary production values have been normalised so that they appear on the same scale as annual integrals.